Remote Sensing of Environment 318 (2025) 114579

Contents lists available at ScienceDirect

Remote Sensing of Environment

journal homepage: www.elsevier.com/locate/rse

A Sentinel-1 SAR-based global 1-km resolution soil moisture data product: Algorithm and preliminary assessment

Dong Fan [a,b,c], Tianjie Zhao [d], Xiaoguang Jiang [e], Almudena García-García [b,c], Toni Schmidt [b,c], Luis Samaniego [f,g], Sabine Attinger [f,g], Hua Wu [h], Yazhen Jiang [h], Jiancheng Shi [i], Lei Fan [j], Bo-Hui Tang [a], Wolfgang Wagner [k], Wouter Dorigo [k], Alexander Gruber [k], Francesco Mattia [l], Anna Balenzano [l], Luca Brocca [m], Thomas Jagdhuber [n,o], Jean-Pierre Wigneron [p], Carsten Montzka [q], Jian Peng [b,c,*]

[a] Yunnan Key Laboratory of Quantitative Remote Sensing, Kunming University of Science and Technology, Kunming, China
[b] Department of Remote Sensing, Helmholtz Centre for Environmental Research - UFZ, Leipzig, Germany
[c] Remote Sensing Centre for Earth System Research – RSC4Earth, Leipzig University, Leipzig, Germany
[d] State Key Laboratory of Remote Sensing Science, Aerospace Information Research Institute, Chinese Academy of Sciences, China
[e] College of Resources and Environment, University of Chinese Academy of Sciences, China
[f] Department of Computational Hydrosystems, Helmholtz Centre for Environmental Research - UFZ, Leipzig, Germany
[g] Institute of Earth and Environmental Science-Geoecology, University of Potsdam, Potsdam, Germany
[h] State Key Laboratory of Resources and Environmental Information System, Institute of Geographical Sciences and Natural Resources Research, Chinese Academy of Sciences, China
[i] National Space Science Center, Chinese Academy of Sciences, China
[j] Chongqing Jinfo Mountain Karst Ecosystem National Observation and Research Station, School of Geographical Sciences, Southwest University, Chongqing, China
[k] Department of Geodesy and Geoinformation, Vienna University of Technology (TU Wien), Vienna, Austria
[l] National Research Council (CNR), Institute for Electromagnetic Sensing of the Environment, Bari, Italy
[m] Research Institute for Geo-Hydrological Protection, National Research Council, Perugia, Italy
[n] Microwaves and Radar Institute, German Aerospace Center (DLR), Weßling, Germany
[o] Institute of Geography, University of Augsburg, Augsburg, Germany
[p] INRAE, UMR1391 ISPA, F-33140, Centre de Bordeaux, Villenave d'Ornon, France
[q] Institute of Bio- and Geosciences: Agrosphere (IBG-3), Forschungszentrum Jülich GmbH, Jülich, Germany

ARTICLE INFO

Edited by: Jing M. Chen

Keywords:
Soil moisture
SAR
Microwave
Sentinel-1
High resolution

ABSTRACT

High spatial resolution of satellite-based soil moisture (SM) data are essential for hydrological, meteorological, ecological, and agricultural studies. Especially, for watershed hydrological simulation and crop water stress analysis, 1-km resolution SM data have attracted considerable attention. In this study, a dual-polarization algorithm (DPA) for SM estimation is proposed to produce a global-scale, 1-km resolution SM dataset (S1-DPA) using the Sentinel-1 synthetic aperture radar (SAR) data. Specifically, a forward model was constructed to simulate the backscatter observed by the Sentinel-1 dual-polarization SAR, and SM retrieval was achieved by minimizing the simulation error for different soil and vegetation states. The produced S1-DPA data products cover the global land surface for the period 2016–2022 and include both ascending and descending data with an observation frequency of 3–6 days for Europe and 6–12 days for the other regions. The validation results show that the S1-DPA reproduces the spatio-temporal variation characteristics of the ground-observed SM, with an unbiased root mean squared difference (ubRMSD) of 0.077 m^3/m^3. The generated 1-km SM product will facilitate the application of high-resolution SM data in the field of hydrology, meteorology and ecology.

* Corresponding author at: Department of Remote Sensing, Helmholtz Centre for Environmental Research - UFZ, Germany.
E-mail address: jian.peng@ufz.de (J. Peng).

https://doi.org/10.1016/j.rse.2024.114579
Received 15 July 2023; Received in revised form 29 November 2024; Accepted 17 December 2024
Available online 8 January 2025

Table 1
Summary of publicly available soil moisture products, with links verified as active in November 2024.

Category	Products	Institution or data center	Spatial coverage	Grid spacing	Temporal coverage	Temporal resolution	Sensor or model	Data link	Reference
Passive microwave based	LPRM SMMR	VUA/NASA	Global	0.25 deg	1978–1987	2–3 days	SMMR	https://www.geo.vu.nl/%7Ejeur/lprm/	(Owe et al., 2008)
	LPRM SSM/I	VUA/NASA	Global	50 km	1987–1999	2–3 days	SMM/I	https://www.geo.vu.nl/%7Ejeur/lprm/	(Owe et al., 2008)
	LPRM TRMM	VUA/NASA	Global	25 km	1997–2015	2–3 days	TMI	https://www.geo.vu.nl/%7Ejeur/lprm/	(Owe et al., 2008)
	LPRM AMSR-E	VUA/NASA	Global	25 km	2002–2011	1–3 days	AMSR-E	https://www.geo.vu.nl/%7Ejeur/lprm/	(Owe et al., 2008)
	AMSR-E L2/L3	JAXA/NASDA	Global	50 km	2002–2011	1–3 days	AMSR-E	https://www.eorc.jaxa.jp/AMSR/index_en.html	(Njoku et al., 2003)
	MCCA AMSR	AIRCAS/TPDC	Global	0.25 deg	2002–2022	1–2 days	AMSR-E/AMSR2	https://data.tpdc.ac.cn/en/data/034b78c9-80d1-47f1-9e19-eeaf2a309010/	(Hu et al., 2023)
	NNsm	THU/AIRCAS	Global	36 km	2002-now	1–2 days	AMSR-E/AMSR2	https://data.tpdc.ac.cn/home	(Yao et al., 2021)
	SMOS L2/L3	ESA	Global	15/25 km	2010-now	1–2 days	SMOS	https://smos-diss.eo.esa.int/oads/access/	(Al Bitar et al., 2017)
	SMOS IC	INRAE BORDEAUX	Global	25 km	2010-now	1–2 days	SMOS	https://ib.remote-sensing.inrae.fr	(Wigneron et al., 2021)
	BEC SMOS L3	EBC	Global	25 km	2010-now	1 days	SMOS	https://bec.icm.csic.es/data/available-products/	(Portabella, 2022a)
	BEC SMOS L4	EBC	Europe	1 km	2010–2022	1 days	SMOS	https://bec.icm.csic.es/data/available-products/	(Portabella, 2022b)
	NNsm FY	AIRCAS/TPDC	Global	25 km	2010-now	1–2 days	FY-3B	https://data.tpdc.ac.cn/home	(Yao et al., 2023)
	AQ3_ANSM	NSIDC	Global	1 deg	2011–2015	1 days	Aquarius	https://nsidc.org/data/aquarius/data	(Bindlish et al., 2015)
	AMSR Unified L2B	NSIDC	Global	25 km	2012-now	1–2 days	AMSR-E/AMSR2	https://nsidc.org/data/au_land/versions/1	(Jackson et al., 2018)
	AMSR-2 L3	JAXA	Global	50 km	2012-now	1–2 days	AMSR2	https://www.eorc.jaxa.jp/AMSR/index_en.html	(Fujii et al., 2009)
	FY-3C/D	NSMC	Global	25 km	2014-now	1–2 days	FY-3C/D	http://satellite.nsmc.org.cn	(Shi et al., 2006 and Kang et al., 2020)
	SMAP_P L2/L3	NSIDC	Global	9/36 km	2015-now	1–2 days	SMAP	https://nsidc.org/data/smap/data	(Entekhabi et al., 2010 O'Neill et al., 2021)
	SMAP-IB	INRAE BORDEAUX	Global	36 km	2015-now	1–2 days	SMAP	https://ib.remote-sensing.inrae.fr	(Li et al., 2022)
	MCCA SMAP	AIRCAS/TPDC	Global	36 km	2015-now	1–2 days	SMAP	https://data.tpdc.ac.cn/en/data/591bb9c8-ed6f-4e86-8372-de1c39ba0283/	(Peng et al., 2024)
	DS-SMAP	UVA/NSIDC	Global	1 km	2015-now	1–2 days	SMAP	https://nsidc.org/data/nsidc-0779/versions/1	(Fang et al., 2022)
Active microwave based	ERS-2	TU/ESA	Global	25/50 km	1991–2011	1–2 days	ERS AMI WS	https://earth.esa.int/web/sppa/activities/multi-sensors-timeseries/scirocco/	(Wagner et al., 1999)
	ASCAT NRT	EUMETSAT H-SAF	Global	10/12.5/25/50 km	2007-now	1–2 days	ASCAT	https://hsaf.meteoam.it/	(Bartalis et al., 2007; Wagner et al., 2013)
	ASCAT NRT DIS	EUMETSAT H-SAF	Europe	1 km	2007-now	1–2 days	ASCAT	https://hsaf.meteoam.it/	(Bartalis et al., 2007; Wagner et al., 2013)
	CLMS SSM	Coperciucs	Europe	1 km	2014-now	1–3 days	Sentinle-1	https://land.copernicus.eu/en/products/soil-moisture	(Bauer-Marschallinger et al., 2019)
	SMAP_A L2/L3	NSIDC	Global	3 km	2015	1–3 days	SMAP	https://nsidc.org/data/smap/data	(Kim et al., 2016)
Multi-sensor merged	ESA CCI	ESA	Global	0.25 deg	1978-now	1 day	ASCAT/SMMR/SSM-I/TMI/AMSR-E/WindSat/FY/	https://archive.ceda.ac.uk/	(Dorigo et al., 2017; Gruber et al., 2019)

(*continued on next page*)

Table 1 (*continued*)

Category	Products	Institution or data center	Spatial coverage	Grid spacing	Temporal coverage	Temporal resolution	Sensor or model	Data link	Reference
							AMSR2/SMOS/ GPM/SMAP		
	CCI 9 km	PANGAEA	Global	9 km	1978–2020	1 day	CCI/SMAP	https://doi.pangaea.de/10.1594/PANGAEA.940409	(Jiang et al., 2022)
	RSSSM	PANGAEA	Global	0.1 deg	2003–2020	10 days	SMAP/ASCAT/ AMSR2/AMSR-E/ SMOS/TMI/FY/ WindSat	https://doi.pangaea.de/10.1594/PANGAEA.940004	(Chen et al., 2021)
	DS-AMSR	TPDC	China	1 km	2003–2023	1 day	AMSR-E/AMSR-2/ MODIS	https://data.tpdc.ac.cn/	(Song et al., 2022)
	SMOPS	NOAA	Global	0.25 deg	2012-now	6 h	GPM/SMAP/GCOM-W1/ MetOp-B	https://www.ospo.noaa.gov/products/land/smops/	(Liu et al., 2016)
	SMAP AP	NSIDC	Global	3/9 km	2015	1–3 days	SMAP Radiometer/ SAR	https://nsidc.org/data/spl3smap/versions/3	(Entekhabi et al., 2016)
	SPL2SMAP_S	NSIDC	Global	1/3 km	2015-now	3–12 days	SMAP/Sentinel-1	https://nsidc.org/data/spl2smap_s/versions/3	(Das et al., 2019)
	GLDAS-2	NASA	Global	0.25 deg	1948–2014	3 h	GLDAS Noah Land Surface Model	https://search.earthdata.nasa.gov/search?q=GLDAS_NOAH025_3H_2.0	(Beaudoing and Rodell, 2020)
	ERA5-Land	ESA	Global	0.1 deg	1950-now	1 h	IFS Model	https://cds.climate.copernicus.eu/datasets/reanalysis-era5-land?tab=overview	(Muñoz Sabater, 2019)
Reanalysis data based	GLEAM	GHENT/ BELSPO/ESA	Global	0.1 deg	1980–2023	1 day	GLEAM-Hydro Model	https://www.gleam.eu/	(Hulsman et al., 2023)
	MERRA-2	NASA	Global	0.5 × 0.625 deg	1980-now	1 day	GEOS ADAS Model	https://climatedataguide.ucar.edu/climate-data/nasas-merra2-reanalysis	(Koster et al., 2015)
	DS-CCI	TPDC/ AIRCAS	Global	1 km	2000–2020	1 day	ESA-CCI/ERA5/ MODIS/ISMN	https://data.tpdc.ac.cn/en/data/30131436-88d1-4be3-8e3d-14905a29d6d6/	(Zheng et al., 2023)
	GLASS	WHU/UMD	Global	1 km	2000–2020	1 day	ERA5-Land/GLASS/ ISMN	http://glass.umd.edu/soil_moisture/	(Zhang et al., 2023)
	SMAP-HB	PU	USA	30 m	2015–2019	6 h	HydroBlocks Model/ SMAP	https://waterai.earth/smaphb/	(Vergopolan et al., 2020, 2021)

1. Introduction

Soil moisture (SM) plays a crucial role in meteorology, hydrology, and ecology. It regulates processes such as precipitation infiltration, vegetation water uptake, and land surface evapotranspiration, making it an indispensable parameter in the soil-vegetation-atmosphere system (SVAT) (Seneviratne et al., 2010). The acquisition of SM data is essential for irrigation guidance (Peng et al., 2021a), estimating crop yields (Dorigo et al., 2017), monitoring droughts and floods (Thober et al., 2015; Boeing et al., 2022), weather forecasting (Samaniego et al., 2019), and long-term terrestrial carbon sequestration (Green et al., 2019).

Neutron scatterometers, electromagnetic sensors, heat pulse probes, and cosmic-ray neutron sensors exemplify ground-based instruments utilized for measuring SM with very high temporal resolution (Nguyen et al., 2017; Kim et al., 2020). However, the SM measurement networks are insufficient and unevenly distributed on a global scale (Peng et al., 2017; Babaeian et al., 2019). Implementing extensive SM measurement networks on a large scale presents logistical impracticalities and economic challenges (Vereecken et al., 2008; Zheng et al., 2022). While SM can be inferred from various land surface model simulations (Loew et al., 2016; Martens et al., 2017), the complexity of the SVAT system and the reliability of input data introduce significant uncertainties in model parameterization and simulation (Samaniego et al., 2013).

Satellite remote sensing technology is an effective means to obtain SM data on a global scale (Wagner et al., 2013). In particular, synthetic aperture radar (SAR) is promising in acquiring all-weather, medium- and high-resolution SM data (Bauer-Marschallinger et al., 2019). The accessibility of freely available SAR data, from sources like the Copernicus Sentinel-1, has significantly boosted the attention and utilization of SAR data for SM monitoring (Balenzano et al., 2021). Nevertheless, the propagation of microwave signals through the SVAT system is inherently intricate owing to the dynamic and spatially heterogeneous of soil and vegetations (Das et al., 2019). Therefore, the key to achieving accurate estimation of SM based on SRA data is to establish a quantitative relationship between the backscatter coefficient and SM and accurately capture the complex interactions within the soil-vegetation system (Kim et al., 2012; Zhu et al., 2020; Wagner et al., 2022).

Until now, numerous studies have delved into SM estimation in bare soil regions by examining the correlation between backscattering coefficient and SM (represented by the dielectric constant) across various frequencies, polarizations, and observation angles (Oh et al., 1992; Dubois et al., 1995). Building upon this foundation, Shi et al. (1997) further refined the polarized backscatter coefficient, the dielectric constant, and the surface roughness power spectrum for bare soil backscatter. Moreover, the field of SAR-based SM estimation has witnessed extensive development through the utilization of theoretical frameworks such as the integral equation model (IEM), the advanced IEM, and the numerical Maxwell model in three dimensions. These models possess the capability to simulate SAR scattering across a broad spectrum of wavelengths and roughness conditions, thereby receiving widespread

citation and application in studies focused on SM retrieval (Fung et al., 1992; Chen et al., 2003; Fung and Chen, 2004; Zhu et al., 2019).

For vegetated areas, observations from optical bands or synchronous ground-based measurements are often used in SAR backscattering models to quantify the effect of vegetation (Wagner et al., 2013; Ma et al., 2019). In this way, SM retrieval methods developed for bare soils are extended to estimate SM beneath the vegetation canopy. A challenge here is that the methods used to quantify the impact of vegetation on SAR backscattering come from specific experimental areas or vegetation phenological phases, and their generalization and transferability across spatial and temporal scales requires further validation. Additionally, reducing the impact of roughness under vegetation coverage on SAR backscattering poses another challenge for SM retrieval (Ma et al., 2020; Palmisano et al., 2020). A good solution is to assume that vegetation and roughness do not change in the short term (Kim and van Zyl, 2009, Kim et al., 2012; Zhu et al., 2019) and to use the difference in multiple SAR backscattering coefficients to represent changes in SM (Wagner, 1998; Pathe et al., 2009; Bauer-Marschallinger et al., 2019; Fan et al., 2022; Wang et al., 2023). However, these methods still have some flaws when applied to estimating global SM. For example, rainfall and human activities can dramatically change roughness in a short period of time. Similarly, it is probable that vegetation has undergone alteration during the two SAR satellite transits, which can result in fluctuations in SAR backscattering and, subsequently, in erroneous SM estimates (O'Neill et al., 2021).

Despite these challenges, there is considerable demand for satellite-based global SM data at 1-km resolution for applications in regional and global meteorology, hydrology, and ecology (Peng et al., 2021a). For instance, numerical weather forecasting systems currently operate at 1-km resolution, underscoring the need for satellite-derived SM datasets with comparable spatial resolution for tasks such as model initialization, data assimilation, and model evaluation (Baatz et al., 2021). However, existing SM products at 1-km resolution with global coverage are typically derived by downscaling coarse-resolution data from passive microwave sources or reanalysis, such as the Soil Moisture Active Passive (SMAP, Entekhabi et al., 2010), the European Space Agency Climate Change Initiative datasets (ESA CCI, Dorigo et al., 2017), and the European Centre for Medium-Range Weather Forecasts Reanalysis v5 (ERA5, Muñoz Sabater, 2019), using auxiliary information such as vegetation index and land surface temperature. Global-scale 1-km resolution SM products based on direct remote sensing inversion remain unavailable (Table 1).

In this study, we propose a novel method for SAR-based SM retrieval. This method builds upon previous research by eliminating the need for synchronous roughness observations and the assumption of constant vegetation and roughness over the short term, allowing for global-scale SM retrieval using only a single snapshot of SAR observations, and producing the first global SAR-based SM product at a 1 km resolution, constraining the error in global SM estimates using C-band SAR to within 0.08 m^3/m^3. The results of this study will facilitate the application of high-resolution SM products in agricultural management and optimization, disaster monitoring and early warning, climate research and modeling, as well as ecological monitoring and protection.

The paper is organized as follows. Section 2 provides a brief introduction to the satellite and ground measurement datasets employed in this study. The details of the SM retrieval algorithm are described in Section 3. Section 4 presents the SM retrieval and validation results. The factors influencing the accuracy of the algorithm are discussed in Section 5. Finally, the conclusions drawn from this research are presented in Section 6.

2. Data and preprocessing

2.1. SAR data

In this study, we utilized the backscattering coefficient data from the interferometric wide swath mode of the Sentinel-1C-band SAR for SM retrieval (Attema et al., 2010). The data was obtained from Google Earth Engine and pre-processed using the Sentinel-1 Toolbox (Veci et al., 2014). It features a spatial resolution of 10 m, with temporal resolution varying across geographic locations, being higher at high latitudes compared to low latitudes (Torres et al., 2012). The dataset comprises three bands: the backscatter coefficients of the VV and VH polarizations, and the angle of incidence. To prepare the SAR data for integration into our SM retrieval algorithm, we conducted additional processing steps.

(1) The incidence angle greatly affects the backscattering coefficient from bare soil and the length of the microwave penetration path through the vegetation layer during SM retrieval. While Sentinel-1 provides the incidence angle based on radar observation, it does not account for the effects of terrain. Therefore, we calculated the local incidence angle (LIA) for each pixel by integrating the observed incidence angle from Sentinel-1 with the Global Multi-resolution Terrain Elevation Data 2010 (Danielson and Gesch, 2011). For right-looking radars such as Sentinel-1, the LIA (θ) can be computed as follows:

$$\theta = arccos(cos\theta_i cos\alpha + sin\theta_i sin\alpha cos(\gamma - \beta)) \quad (1)$$

where θ_i is the SAR incidence angle,γ is the SAR azimuth angle, α and β denote the slope and aspect of the ground, respectively.

(2) To mitigate the influence of terrain on backscattering coefficients, we applied the method proposed by Bauer-Marschallinger et al. (2021) to normalize Sentinel-1 backscattering coefficients to an LIA of 38°. It can be expressed as:

$$\sigma^0(38) = \sigma^0(\theta) - \zeta(\theta - 38^0) \ \ [dB] \quad (2)$$

where $\sigma^0(38)$ is the normalized backscatter in dB, σ^0 is the backscatter from Sentinel-1 observations, θ is the LIA, and ζ is an empirical parameter, where $\xi = -0.13$ (Bauer-Marschallinger et al., 2021).

(3) Extremely high or low values of backscattering coefficient values are less likely to contain credible SM information and should be discarded. In this study, pixels with a backscatter less than −20 dB or greater than −5 dB in VV polarization were masked. The threshold of −5 dB is derived from a qualitative estimate of backscatter in urban areas, while the threshold of −20 dB is based on a conservative estimate of sensor noise (−22 dB) (Bauer-Marschallinger et al., 2019).

(4) The backscattering coefficients are converted from decibels to linear units to preserve the original SAR signal. Subsequently, the data were aggregated form a 10 m resolution to 1 km by averaging. Although this averaging method overlooks the nonlinear nature of signal reflections in SAR data, it is commonly used in large-area SAR data processing because it indirectly reduces random noise, thereby enhancing the effect of SM on the backscatter coefficient (Bauer-Marschallinger et al., 2019; Fan et al., 2022; Wang et al., 2023). Additionally, the processed SAR data for each day are mosaicked separately according to their respective ascending and descending orbits.

2.2. Vegetation data

The vegetation layer is a critical component that significantly influences backscatter signals (Kim et al., 2012; Qiu et al., 2019). In this study, Normalized Difference Vegetation Index (NDVI) data from the Moderate Resolution Imaging Spectroradiometer (MODIS) MOD13A2 V6.1 and the annual land use and land cover dataset derived from the MODIS MCD12Q1 V6 International Geosphere-Biosphere Programme (IGBP) classification scheme were used to estimate the vegetation water content (VWC) for each grid (O'Neill et al., 2021):

Table 2
Basic information of the ISMN networks used in this study. The land cover types derived from the IGBP classification include evergreen needleleaf forest (ENF), evergreen broadleaf forest (EBF), deciduous broadleaf forest (DBF), mixed forest (MF), closed shrubland (CS), open shrubland (OS), woody savanna (WS), savanna (S), grassland (G), permanent wetlands (PW), croplands (C), urban and built-up land (UB), cropland/natural vegetation mosaics (CNVM), permanent snow and ice (PSI), barren or sparsely vegetated (B), and water bodies (W).

Network	Country	Number of sites	Land cover	Reference
AMMA-CATCH	Benin, Niger, Mali	10	G(6), C(4)	(Lebel et al., 2009)
ARM	USA	51	G(21), C(30)	(Cook, 2016)
BIEBRZA_S-1	Poland	18	S(18)	(Musial et al., 2016)
FLUXNET-AMERIFLUX	USA	3	S(1), G(1), C(1)	(https://ameriflux.lbl.gov/)
FR_Aqui	France	3	WS(3)	(Al-Yaari et al., 2018)
HOAL	Austria	41	WS(1), C(40)	(Bloeschl et al., 2016)
HOBE	Denmark	54	ENF(3), S(18), C(25), CNVM(8)	http://www.hobe.dk/
MAQU	China	13	G(13)	(Su et al., 2011)
NAQU	China	7	G(7)	(Su et al., 2011)
OZNET	Australia	19	G(10), C(9)	(Smith et al., 2012)
PBO_H2O	USA	124	EBF(1), CS(1), OS(10), WS(2), S(3), G(85), C(9), (1), B(12)	(Larson et al., 2008)
REMEDHUS	Spain	20	OS(5), G(1), C(14)	(Gonzalez-Zamora et al., 2019)
RISMA	Canada	66	G(3), C(63)	(http://aafc.fieldvision.ca/)
RSMN	Romania	14	C(14)	(Ojo et al., 2015)
SCAN	USA	199	ENF(1), EBF(3), DBF(14), OS(10), WS(28), S(19), G(65), C(52), CNVM(1), B(6)	(Schaefer et al., 2007)
SMN-SDR	China	33	G(31), C(2)	(Zhao et al., 2020)
SMOSMANIA	France	27	ENF(1), WS(8), S(7), C(10), CNVM(1)	(Albergel et al., 2008)
SNOTEL	USA	362	ENF(24), MF(2), OS(7), WS(51), S(76), G(201), B(1)	(Serreze et al., 2001)
SOILSCAPE	USA	20	OS(3), S(6), G(11)	(Moghaddam et al., 2010)
TAHMO	Ghana	3	WS(2), C(1)	(https://tahmo.org/)
TERENO	Germany	14	MF(2), S(3), C(9)	(Zacharias et al., 2011)
TWENTE	Netherlands	28	S(18), G(3), C(1), CNVM(6)	(Van der Velde et al., 2023)
TxSON	USA	40	S(7), G(33)	(Caldwell et al., 2019)
USCRN	USA	104	ENF(3), DBF(3), MF(2), CS(1), OS(7), WS(20), S(11), G(45), C(7), CNVM(3), B(2)	(Bell et al., 2013)
XMS-CAT	Spain	17	ENF(1), S(8), G(3), C(5)	(https://visors.icgc.cat/mesuras ols)
iRON	USA	9	S(3), G(6)	(Osenga et al., 2021)

$$m_v = \left(1.9134NDVI^2 - 0.3215NDVI\right) + S\left(NDVI_{ref} - 0.1\right)/(1 - 0.1) \quad (3)$$

where m_v is the VWC. For croplands and grasslands, the $NDVI_{ref}$ is the current NDVI, and for other land covers, the $NDVI_{ref}$ denotes the annual maximum NDVI. S is the function of the sapwood, leaf area, and vegetation height. In this study, the look-up table from the research of O'Neill et al. (2021) was used to obtain the S of each pixel based on the IGBP classification.

To obtain globally seamless VWC data, we applied climatological processing to global MODIS NDVI data from 2000 to 2016 (Jackson et al., 2011; Bindlish et al., 2011; O'Neill et al., 2021). This processing generated 36 global seamless NDVI datasets, each with a 10-day temporal resolution and a 1 km spatial resolution, representing the average vegetation state at specific times of the year. While this average state may not fully capture actual conditions during SM retrieval, it helps address substantial data gaps in NDVI caused by clouds and rain, serving as a valuable supplementary dataset for global SM retrieval in the SMAP single-channel algorithm (O'Neill et al., 2021).

2.3. Soil texture data

Soil texture is a critical factor influencing soil dielectric properties (Ulaby et al., 2015). In this study, the soil clay fraction was used as an auxiliary input to a dielectric constant model to quantify the relationship between SM and dielectric constant across different soil textures. The clay fraction dataset from OpenLandMap (Hengl, 2018), which provides global clay fraction data at a depth of 0–10 cm for each 250 m grid cell, was used. This dataset was aggregated to a 1 km scale by averaging to match the spatial resolution of other datasets used in SM retrieval.

2.4. Snow cover and surface temperature data

Snow cover and surface temperature data are utilized to exclude pixels affected by snow and soil freezing, as they are not suitable for SM retrieval. These data are derived from the land component of the ERA5-Land (Muñoz Sabater, 2019), which provides snow cover and surface temperature measurements every hour for each 9 km grid. Specifically, data at 6:00 AM and 6:00 PM were employed to mask the retrieved SM of the descending and ascending orbits, respectively.

2.5. SM data

The SMAP enhanced L3 radiometer global daily 9 km EASE-Grid SM product version 5 (L3_SM_P_E, O'Neill et al., 2021) are used to pre-calibrate the parameters of the proposed algorithm in this study. This data provides SM data for each 9-km grid every 1–2 days, in which the water bodies, cities, snow cover, and frozen pixels are removed in advance. Extensive verification shows that it is one of the most accurate global SM datasets currently available, with a root mean square error (RMSE) of less than 0.04 m^3/m^3 (Peng et al., 2021b; Beck et al., 2021).

Four representative global 1 km SM products were compared with the SM retrieved by the algorithm proposed in this study: (1) the global 1 km spatiotemporally seamless SM product (GLASS), synthesized using ERA5-Land reanalysis data, ground-based SM data, and auxiliary datasets, such as land surface temperature, albedo, NDVI, leaf area index, and elevation (Zhang et al., 2023); (2) the global daily surface SM product on a 1-km grid, derived from gap-filling and downscaling of the ESA CCI datasets (DS-CCI, Zheng et al., 2023); (3) the 1 km SM product obtained by downscaling the SMAP enhanced L2 radiometer half-orbit SM product using thermal inertia theory, with land surface temperature and NDVI data (DS-SMAP, Fang et al., 2022); and (4) the 1-km

resolution SM product, which synergistically uses SMAP L-band radiometer and Sentinel-1C-band SAR data through the SMAP active-passive algorithm (SPL2SMAP_S, Das et al., 2019).

Moreover, SM data from ground-based probes of the International Soil Moisture Network (ISMN, Dorigo et al., 2021) were adopted to validate the proposed SM retrieval algorithm. ISMN serves as a data hosting and sharing center for global ground-based SM data and is often used as the "true value" in the verification of remote sensing and model-derived SM products (Dorigo et al., 2011). In this study, measurements from the topmost probes (0–5 cm) covering the period 2016–2022 were considered as the reference SM. Only SM data identified as "good" by the quality control file were used. A total of 1299 ground observation stations from 26 networks were selected for this study, and the basic information of these in-situ observations is presented in Table 2.

3. Methodology

To enhance the applicability of the algorithm across various land surface conditions, we developed a forward model aimed at quantifying the relationship between SM and SAR backscattering coefficients. Subsequently, the SM was retrieved as the value that minimizes the difference between the backscattering coefficient obtained from the forward model and the observation acquired from Sentinel-1. The specific SM retrieval algorithm is described below.

3.1. Forward model description

In this study, the water-cloud model (Attema and Ulaby, 1978) was applied to quantify the effects of SAR backscattering coefficients affected by vegetation. In this model, the vegetation layer is characterized as a homogeneous attenuating medium with a uniform thickness that remains consistent horizontally. As a result, the total backscattering coefficients can be attributed to direct backscattering by vegetation, soil backscattering after being attenuated twice by vegetation, and direct soil backscattering.

$$\sigma_{pq}^0 = \sigma_{pqv}^0 + L_{pq}^2 \sigma_{pqs}^0 \tag{4}$$

$$\sigma_{pqv}^0 = A_{pq} m_{pqv} cos\theta \left(1 - L_{pq}^2\right) \tag{5}$$

$$L_{pq}^2 = exp\left(-2\tau_{pq} sec\theta\right) \tag{6}$$

$$\tau_{pq} = b_{pq} m_v \tag{7}$$

Where pq is the polarization of vertical and horizontal, σ_{pq}^0 is the total SAR backscattering coefficients, σ_{pqv}^0 and σ_{pqs}^0 denotes the direct backscattering coefficients for vegetation and soil, respectively. L_{pq} is the vegetation transmissivity, θ represents LIA (°), τ_{pq} is the vegetation optical depth, A_{pq} and b_{pq} are parameters in connection with the vegetation layer, and m_v is the VWC (kg/m^2), which can be estimated from the land cover types and NDVI (Eq. 3, O'Neill et al., 2021).

The Oh model (Oh et al., 1992) was utilized to quantify the backscattering coefficients of bare soil. This model treats the backscattering coefficients of bare soil as a function of SM, surface roughness, LIA, and SAR frequency.

$$\sigma_{vvs}^0 = \frac{g cos^3\theta [\Gamma_v(\theta) + \Gamma_h(\theta)]}{\sqrt{r}} \tag{8}$$

$$\sigma_{hhs}^0 = r\sigma_{vvs}^0 \tag{9}$$

$$\sigma_{hvs}^0 = u\sigma_{vvs}^0 \tag{10}$$

where σ_{vvs}^0, σ_{hhs}^0, and σ_{hvs}^0 are soil backscattering coefficients in three different polarizations, v and h are the polarization of vertical and horizontal, and r, u and g are empirical parameters, which could be calculated by:

$$r = \frac{\sigma_{hh}^0}{\sigma_{vv}^0} = \left[1 - \left(\frac{2\theta}{\pi}\right)^{1/3\Gamma_0} exp(-ks)\right]^2 \tag{11}$$

$$u = \frac{\sigma_{hv}^0}{\sigma_{vv}^0} = 0.23\sqrt{\Gamma_0}[1 - exp(-ks)] \tag{12}$$

$$g = 0.7\left[1 - exp\left(-0.65(ks)^{1.8}\right)\right] \tag{13}$$

$$s = \sqrt{\frac{1}{N}\left(\sum_{i=1}^{N} z_i^2 - N\cdot\bar{z}^2\right)} \tag{14}$$

$$k = 2\pi/\lambda \tag{15}$$

where k is the SAR wavenumber, λ is the wavelength, and s is the root-mean-square height of the soil surface, which can be calculated from the height z_i and the average height $\bar{z}$ of the N sampling points. Γ_0, Γ_v, and Γ_h is the Fresnel reflection coefficient of nadir and in the polarization of v and h, respectively, which could be calculated by:

$$\Gamma_0 = \left|\frac{1 - \sqrt{\varepsilon}}{1 + \sqrt{\varepsilon}}\right|^2 \tag{16}$$

$$\Gamma_v = \left|\frac{\varepsilon\cdot cos\theta - \sqrt{\varepsilon - sin^2\theta}}{\varepsilon\cdot cos\theta + \sqrt{\varepsilon - sin^2\theta}}\right|^2 \tag{17}$$

$$\Gamma_h = \left|\frac{cos\theta - \sqrt{\varepsilon - sin^2\theta}}{cos\theta + \sqrt{\varepsilon - sin^2\theta}}\right|^2 \tag{18}$$

where ε represents the dielectric constant (real part) of bare soil, which can be calculated using a variety of dielectric models (Loor, 1968; Topp et al., 1980; Wang and Schmugge, 1980; Dobson et al., 1985; Mironov et al., 2004; Hallikainen et al., 2007).

In this study, we utilized the Mironov model (Mironov et al., 2004, 2009) to quantify the dielectric constant of soil. This model treats the dielectric constant of soil as a volume-weighted average of the dielectric constants of various soil constituents, such as mineral solids, air, and SM. Additionally, it distinguishes between bound and free SM, which is expressed as follows:

$$\sqrt{\varepsilon} = \begin{cases} \sqrt{\varepsilon_d} + \left(\sqrt{\varepsilon_b} - 1\right)m_s, & m_s \le m_{st} \\ \sqrt{\varepsilon_d} + \left(\sqrt{\varepsilon_b} - 1\right)m_{st} + \left(\sqrt{\varepsilon_u} - 1\right)(m_s - m_{st}), & m_s \ge m_{st} \end{cases} \tag{19}$$

where the ε_b and ε_u are the dielectric constant of bound and unbound SM, respectively. ε_d is the dielectric constant of the absolutely dry soil, m_{st} is the volumetric moisture of the soil, and m_{st} is the maximum bound SM fraction. It is a function of SAR frequency, soil texture (clay fraction), and SM (see Appendix A).

3.2. Forward model calibration

The forward model can be employed to simulate the backscattering coefficients corresponding to different SM levels once the semi-empirical vegetation parameters A, b, and the soil surface roughness parameter s have been determined using Eqs. (4) ~ (19). In the SMAP single-channel algorithm, parameters A, b, and s are defined as constants for each land cover (O'Neill et al., 2021). However, due to differences in spatial resolution and wavelength between Sentinel-1 and SMAP, these parameters cannot be directly applied in this study. Furthermore, the insufficient and uneven distribution of ground sites makes global-scale

Table 3
Summary of input parameters.

Parameter name	Symbol	Threshold	Iteration step size
Frequency	f	5.405 (GHz)	–
Local incidence angle	θ	38 (°)	–
Soil moisture	m_s	0.02–0.60 (m^3/m^3)	0.01 (m^3/m^3)
Clay fraction	C	0–62 (%)	–
Surface roughness	s_0	0–6 (cm)	0.1 (cm)
Vegetation water content	m_v	0–17.8 (kg/m^2)	–
Parameter of vegetation type A	A_0	0–1	0.01
Parameter of vegetation type b	b_0	0–1	0.01

model parameter calibration based on ground measurements impractical. Therefore, the SMAP L3_SM_P_E product, characterized by relatively high spatial resolution (9 km) and accuracy (RMSD <0.04 m^3/m^3), was used to calibrate the forward model parameters.

In this study, the backscattering coefficients at the time of the Sentinel-1 overpass were simulated based on the forward model, and parameters A, b, and s were calibrated by minimizing the discrepancy between simulated and observed backscattering coefficients. The cost function (C_{cal}) is defined as follows:

$$C_{cal}(A_0, b_0, s_0) = \frac{1}{2}\sum_{pq=vv,vh}\sqrt{\frac{1}{n}\sum_{t=1}^{n}\left(\widehat{\sigma}^0_{pq}(A_0, b_0, s_0) - \sigma^0_{pq}\right)^2} \quad (20)$$

where A_0, b_0, and s_0 are the calibrated vegetation and surface roughness parameters in the forward model, pq is the polarization mode, t is the Sentinel-1 overpass index, n is the number of simulated and observed backscatter, and $\widehat{\sigma}^0_{pq}$ is the backscattering coefficients simulated by the forward model, while σ^0_{pq} represents that of the normalized Sentinel-1 observations.

The pixel-by-pixel calibration process was conducted at a resolution of 9 km, corresponding to the resolution of the SMAP L3_SM_P_E product. Prior to calibration, Sentinel-1 backscattering data and ancillary data such as VWC and soil clay fraction were aggregated to the coarse resolution of 9 km by averaging. This approach preserves the accuracy of the SMAP L3_SM_P_E data in the forward model and greatly improves calibration efficiency. Unlike typical machine learning methods that require extensive parameter calibration, the model used in the study incorporates a specific physical mechanism and requires only a minimum of one year's data, cover a complete vegetation growth and withering cycle, for accurate calibration. The specific calibration procedure can be expressed as follows:

(1) Using the SMAP L3_SM_P_E as input, along with soil clay fraction and vegetation data, iterate the parameters A_0, b_0, and s_0 with a small step (as shown in Table 3) to simulate the backscatter under specific conditions of SM, VWC, LIA, SAR frequency, and polarization.
(2) Compute the disparity between the backscatter values obtained from forward model simulations and normalized Sentinel-1 observations in both VV and VH polarizations across various parameters A_0, b_0, and s_0 at each overpass time.
(3) Iterate through the aforementioned steps using all data from 2016 and 2017 as input. Calculate the average forward model simulation error for all Sentinel-1 overpasses corresponding to each parameter A_0, b_0, and s_0. Subsequently, identify the parameter combination A_0, b_0, and s_0 associate with the minimum overall error (as defined in Eq. 20) as the optimal calibration result.
(4) Traverse each 9 km grid globally to calibrate the parameters A_0, b_0, and s_0.

3.3. SM retrieval

Once the vegetation parameters are calibrated, only SM and surface roughness remain as the two variables needing estimation. However, the simultaneous estimation of SM and surface roughness is sensitive to sensor noise because the observed backscattering of VV and VH polarizations is not completely independent (Konings et al., 2015). To address this issue, Fan et al. (2022) proposed a dual-temporal dual-channel algorithm that simultaneously estimates SM at the time of two adjacent observations and the surface roughness over a specified time interval using four data sets obtained from two adjacent dual-channel SAR observations. In addition, Kim et al. (2012), Zhu et al. (2019), and Wang et al. (2023) also utilized multiple observations to reduce the uncertainty in SM retrieval.

Based on the above research, we proposed a dual-polarization algorithm (DPA) that can estimate both SM and surface roughness simultaneously using only a single snapshot of dual-polarization SAR data. Specifically, the DPA algorithm enables the simultaneous retrieval of SM and surface roughness using dual-polarization SAR data by: I) limiting SM and surface roughness thresholds (Table 3), what's more, II) assuming that the surface roughness at the time of the SAR observation (s) should be close to the "long-term" roughness (s_0) of that pixel. Consequently, at each Sentinel-1 observation time, SM and surface roughness can be estimated concurrently by minimizing the discrepancy between the backscattering coefficients derived from the calibrated forward model and the Sentinel-1 observations in both VV and VH polarizations. The cost function is (C_{ret}) defined as follows:

$$C_{ret}(m_s, s) = \sum_{pq=vv,vh} w\left[\frac{\widehat{\sigma}^0_{pq}(m_s, s) - \sigma^0_{pq}}{\sigma^0_{pq}}\right]^2 + (1-w)\left(\frac{s - s_0}{s_0}\right)^2 \quad (21)$$

where m_s and s are the SM and surface roughness that are intended to be retrieved, s_0 is the "long-term" roughness parameter of the pixel obtained by the calibration process, and w represents the weight of the residual of backscattering coefficients and roughness. This wight is an empirical parameter and is taken as 0.5 here to ensure that the retrieved SM is more continuous in temporal and spatial scales. Since there is no need to process multiple sets of data simultaneously, this approach significantly reduces the complexity of the multitemporal algorithm, making it suitable for the retrieval of long-term SM on a global scale. The specifics of the proposed retrieval algorithm are as follows:

(1) To match the grid size of the SAR backscatter, VWC, and clay fraction data, we interpolate the calibrated parameters from a spatial resolution of 9 km to 1 km using the nearest neighbor approach.
(2) Utilizing the calibrated forward model, SM and surface roughness are iterated with a small step size (Table 3) to simulate a series of backscattering coefficients and calculate the cost function value (Eq. 21). The SM corresponding to the minimum cost function value is then considered as the retrieved result.
(3) For each 1 km grid and during each Sentinel-1 overpass time, repeat the process described in step 2 to obtain the long-term 1-km resolution SM.
(4) Pixels with snow cover exceeding 10 %, a surface temperature below 275.15 K, or a cost function value (Eq. 20) exceeding 1 were masked to mitigate the effects of snow cover, ground freezing, or calibration errors (Fig. B2a). The schematic diagram illustrating the proposed SM retrieval method is depicted in Fig. 1.

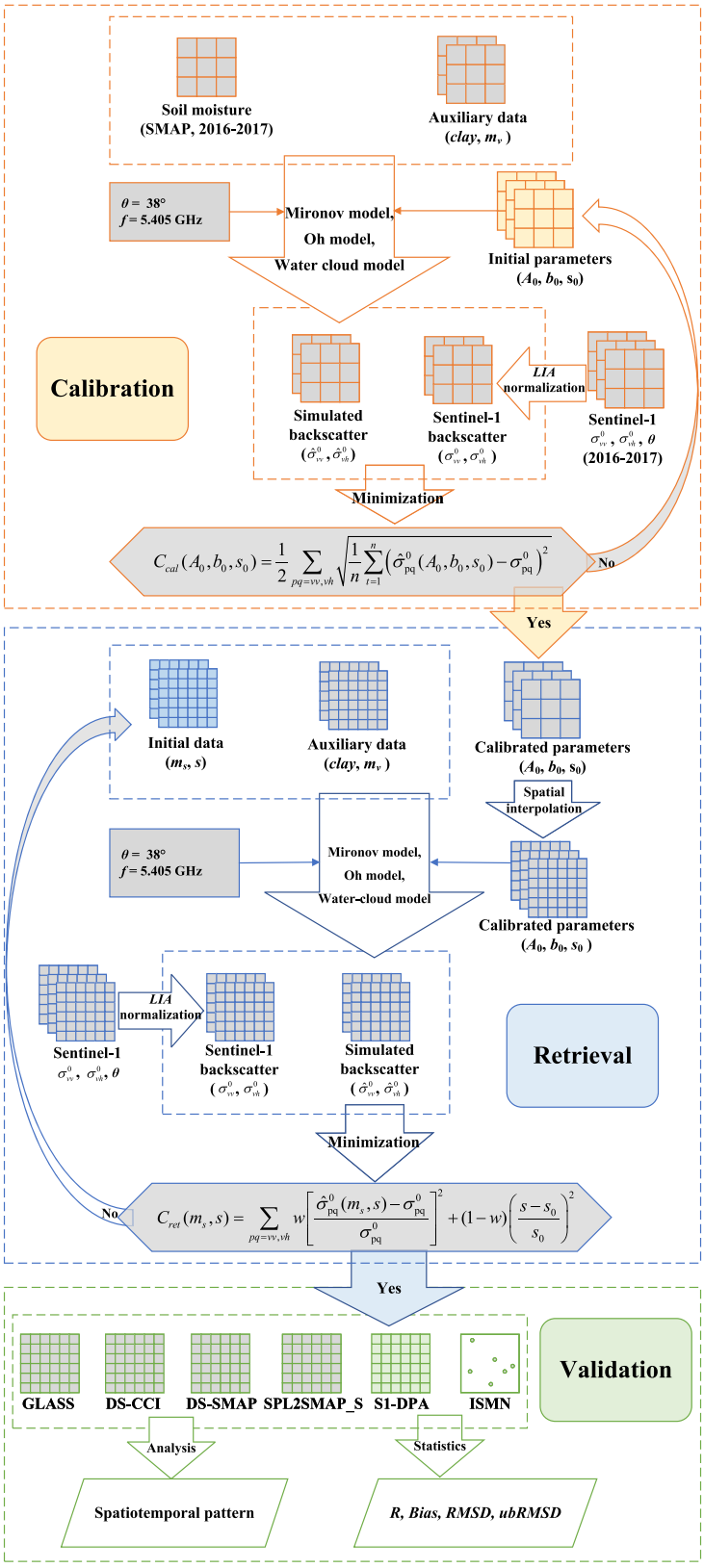

Fig. 1. Flowchart illustrating the proposed SM retrieval method. (1) In the calibration part, by iterating the parameters A_0, b_0, and s_0 and using SMAP passive SM data as input, the cost function C_{cal} is minimized at 9-km resolution. (2) In the retrieval part, the SM and surface roughness must be iterated until the cost function C_{ret} is minimized at a resolution of 1 km (see Appendix B). (3) In the validation part, the SM derived from the proposed method (S1-DPA) is compared with SM data from the machine learning-based product (GLASS), downscaled reanalysis product (DS-CCI), downscaled passive microwave product (DS-SMAP), joint passive and active microwave product (SPL2SMAP_S), and ground measurements (ISMN) to analyze spatio-temporal patterns and calculate the correlation coefficient, bias, root mean square difference, and unbiased root mean square difference.

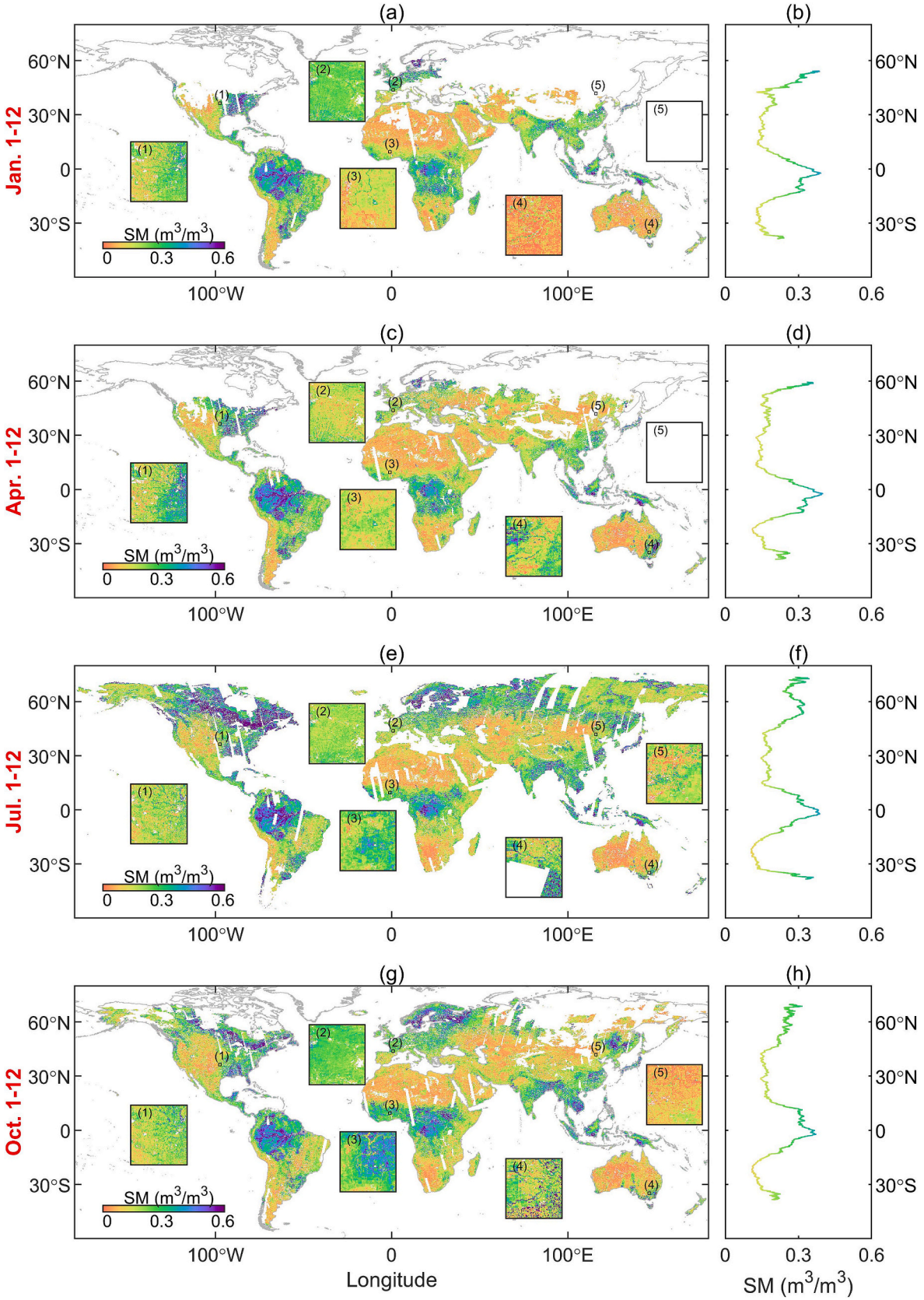

Fig. 2. Twelve-day coverage of S1-DPA SM and its latitudinal variations from 1st to 12th of January, April, July, and October in 2020. The zoom-in views of the selected sub-regions over different ISMN networks: (1) ARM network in America, (2) SMOSMANIA network in Europe, (3) TAHMO network in Africa, (4) OZNET network in Australia, and (5) SMN-SDR in China.

Table 4
Temporal correlation R, bias, RMSD, and ubRMSD between S1-DPA and ISMN from 2016 to 2022. The number of sites and data used for each network are provided in the last two columns of the table. Sites with an effective data amount of less than 10 and networks with an effective number of sites of less than 3 are excluded.

Network	Median R	Median bias (m^3/m^3)	Median RMSD (m^3/m^3)	Median ubRMSD (m^3/m^3)	Number of Sites	Data pairs
AMMA-CATCH	0.547	0.078	0.092	0.037	10	892
ARM	0.370	−0.021	0.133	0.109	51	9877
BIEBRZA_S-1	0.215	−0.193	0.215	0.080	18	2625
FLUXNET-AMERIFLUX	0.739	0.004	0.115	0.104	3	700
FR_Aqui	0.656	0.147	0.156	0.050	3	1892
HOAL	0.470	−0.081	0.127	0.090	41	3987
HOBE	0.549	0.044	0.113	0.088	54	12,984
MAQU	0.663	0.035	0.125	0.081	13	372
NAQU	0.600	0.059	0.109	0.085	7	291
OZNET	0.575	0.040	0.116	0.107	19	1843
PBO_H2O	0.497	−0.025	0.078	0.055	124	6064
REMEDHUS	0.414	0.020	0.089	0.061	20	11,628
RISMA	0.303	0.003	0.158	0.135	66	3978
RSMN	0.460	0.087	0.116	0.080	14	8229
SCAN	0.290	0.015	0.105	0.078	199	25,749
SMN-SDR	0.411	−0.023	0.087	0.055	33	1329
SMOSMANIA	0.405	−0.003	0.095	0.077	27	16,616
SNOTEL	0.267	−0.010	0.106	0.080	362	36,976
SOILSCAPE	0.515	−0.002	0.100	0.058	20	252
TAHMO	0.613	0.081	0.093	0.046	3	450
TERENO	0.515	−0.058	0.105	0.074	14	8766
TWENTE	0.577	−0.003	0.104	0.084	28	13,627
TxSON	0.659	−0.019	0.073	0.044	40	6015
USCRN	0.402	0.012	0.097	0.072	104	18,532
XMS-CAT	0.330	0.042	0.096	0.067	17	4429
iRON	0.231	0.003	0.052	0.033	9	784
Median for all stations	0.377	−0.003	0.105	0.077	–	–

4. Results

4.1. Spatio-temporal pattern of the S1-DPA data

The SM data product derived from Sentinel-1 DPA has a spatial resolution of 1 km, covering the period from 2016 to 2022. This dataset matches the swath width (250 km) of Sentinel-1's interferometric wide swath mode, with revisit intervals ranging from 6 to 12 days depending on the region (Bauer-Marschallinger et al., 2019). Synthesizing S1-DPA SM data every 12 days enables coverage of most land areas (Fig. 2). Notably, there is more valid data in July than in January, largely due to temperature and snow cover effects that render many pixels unsuitable for SM retrieval during winter. This limitation is especially evident in high-latitude and high-altitude regions, such as Siberia and the Qinghai-Tibet Plateau. The theoretical minimum value of this dataset is 0.02 m^3/m^3, primarily observed in desert regions, while the maximum value is 0.6 m^3/m^3, found mainly in tropical rainforests and sub-polar areas. To illustrate the spatiotemporal variations in detail, we selected regions from five ground-based SM observation networks across different continents. For example, within the TAHMO network (labeled as (3) in Fig. 2), soil is relatively dry in January and April, becoming increasingly moist in July and October.

4.2. Accuracy verification of the S1-DPA products

We compared the S1-DPA product with in-situ SM data from 1299 sites across 26 networks, covering the period from 2016 to 2022 (Table 4). For each site, the correlation coefficient (R), bias, root mean square deviation (RMSD), and unbiased root mean square deviation (ubRMSD) were calculated. To mitigate extreme anomalies or reconcile positive and negative data errors between stations, we calculated the median values for each network and all involved stations. Overall, the S1-DPA product shows a R of 0.377 with in-situ SM, a bias of −0.003 m^3/m^3, an RMSD of 0.105 m^3/m^3, and an ubRMSD of 0.077 m^3/m^3.

Fig. 3 illustrates the accuracy of ascending and descending orbit data from the S1-DPA product across all ground observation networks. The S1-DPA descending orbit data correspond to a local time of 6:00 AM at ground station locations, while the ascending orbit data correspond to 6:00 PM. Due to the site location and observation mode of Sentinel-1, S1-DPA does not provide effective descending estimates at some stations, such as those included in the AMMA-CATCH network, or ascending estimates at stations in the OZNET network. The overall accuracy (median) of S1-DPA descending orbit data is $R = 0.387$, with a bias of −0.004 m^3/m^3, RMSD of 0.102 m^3/m^3, and ubRMSD of 0.075 m^3/m^3. For ascending orbit data, $R = 0.370$, bias is −0.003 m^3/m^3, RMSD is 0.108 m^3/m^3, and ubRMSD is 0.079 m^3/m^3.

To validate the performance of the S1-DPA product in depicting actual SM changes over time, we selected four ground observation networks to illustrate the temporal trends of S1-DPA SM. These trends were compared between ascending (blue dots) and descending (pink dots) observations, as well as in-situ SM measurements (black lines) from 2016 to 2022 (Fig. 4). In high SM conditions, the S1-DPA product may overestimate actual SM, as observed in the OZNET network. In this case, the ubRMSD is relatively large, at 0.096 m^3/m^3, but the correlation with in-situ measurements remains high, at 0.737. Overall, the product accurately represents temporal variations in SM in most cases, for both ascending and descending orbits.

4.3. Comparison with existing SM products

Fig. 5 shows the distribution of the temporal average and annual seasonal amplitude (SA) for five typical SM products with a spatial resolution of 1 km in 2020. SA is defined as the difference between the maximum SM value (expressed as the 95th percentile) and the minimum SM value (expressed as the 5th percentile) after applying a 45-day sliding average (Konings et al., 2017; Li et al., 2022; Peng et al., 2024). As shown in Fig. 5a, the spatial pattern of the GLASS product appears relatively smooth, with lower SM levels in tropical and subarctic zones. This stability may result from the integration of multiple datasets, especially reanalysis data, within the GLASS product, which could dampen peak SM values (Dorigo et al., 2017). The DS-CCI data at low and mid-latitudes primarily stem from remotely sensed observations,

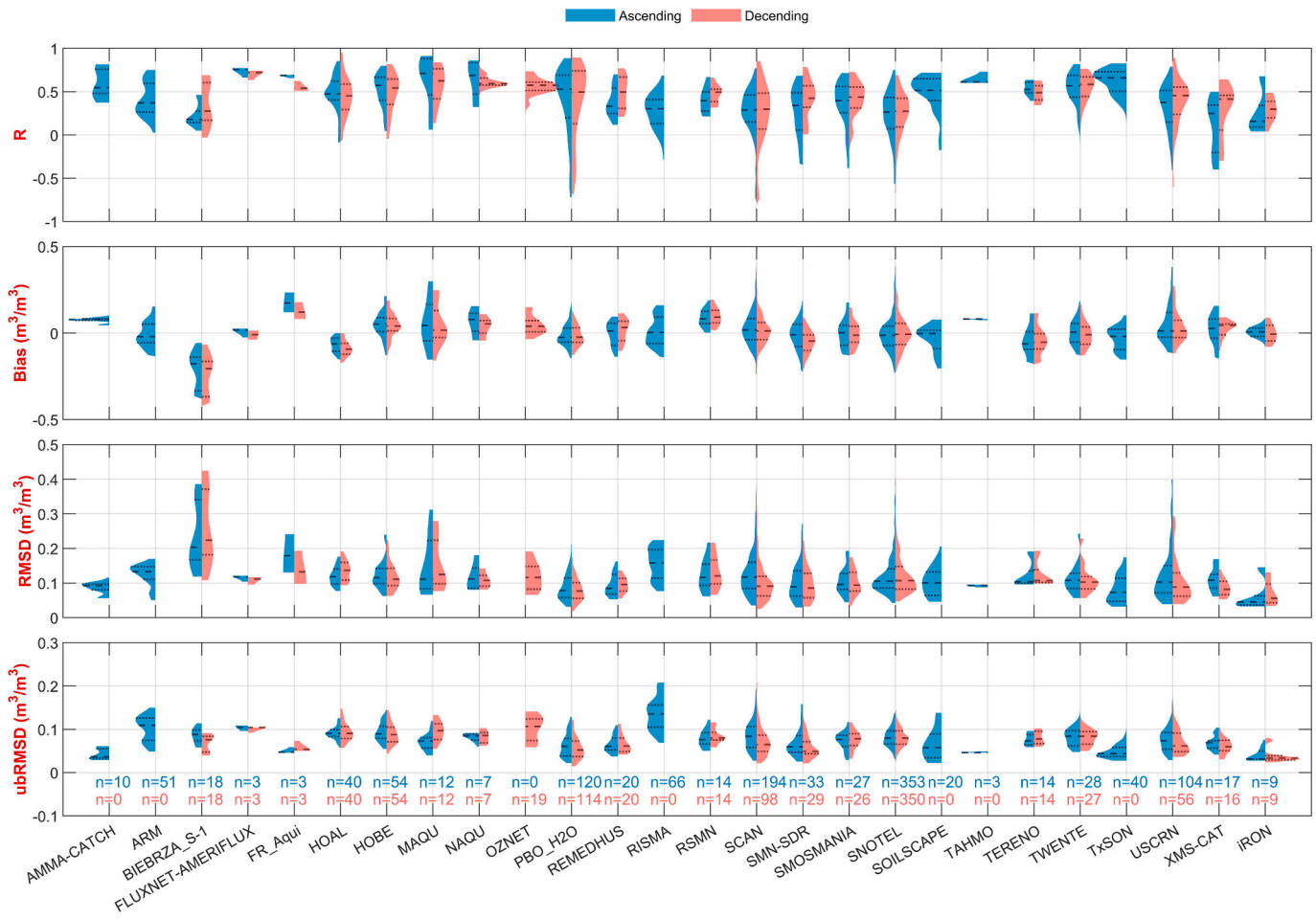

Fig. 3. Violin plot summarizing R, bias, RMSD, and ubRMSD between the S1-DPA and the ISMN from 2016 to 2022, based on data from ascending (blue) and descending orbits (pink). The 25 % percentile, median, and 75 % percentile are shown by the horizontal dotted lines. Due to the limitations of Sentinel-1's acquisition mode, a given station may have only ascending observations, only descending observations, or both. The numbers shown below indicate the number of sites included in the analysis. Networks with an effective number of sites less than 3 are excluded. (For interpretation of the references to colour in this figure legend, the reader is referred to the web version of this article.)

allowing for the visualization of high SM levels in tropical rainforests. In contrast, high-latitude areas are supplemented with reanalysis data, leading to a relatively smooth representation (Fig. 5c). By comparison, the DS-SMAP, SPL2SMAP_S, and S1-DPA products are predominantly derived from remote sensing observations. As a result, these products display higher SM levels in regions such as central South America, Africa, Southeast Asia, and northern North America and Europe (Fig. 5e, g, and i). Regarding spatial variability of SA, GLASS and DS-CCI exhibit slight SM variability, particularly in high-latitude regions, contrasting with the more pronounced SA seen in SPL2SMAP_S and the moderate fluctuations in DS-SMAP and S1-DPA. Notably, only SPL2SMAP_S displays significant SA in tropical rainforest regions, including Central America, Central Africa, and Southeast Asia.

Fig. 6 displays the R and ubRMSD between the S1-DPA product and four typical SM products at a 1 km spatial resolution for 2020. High correlation values are observed in tropical and subtropical monsoon regions, including African and South American grasslands, as well as much of India and Indochina. Conversely, barren regions with extremely low SM levels, such as the Sahara Desert, Arabian Peninsula, and west-central Australia, exhibit notably low R values and ubRMSD. In high-latitude areas, such as northern North America and northern Europe, R values are relatively low while ubRMSD is high, especially for the GLASS and DS-CCI products. Overall, S1-DPA data show the highest agreement with DS-SMAP (Fig. 6e and f), with a median R value of 0.373 and a ubRMSD of 0.056 m^3/m^3. In contrast, the largest relative differences are found between S1-DPA and SPL2SMAP_S (Fig. 6g and h), with a median R value of 0.319 and a ubRMSD of 0.077 m^3/m^3, corresponding to the pronounced spatial variability of SPL2SMAP_S shown in Fig. 5h.

The SMOSMANIA network area serves as an example to characterize the detailed spatial and temporal distribution of the five 1-km-resolution SM products (Fig. 7). All products effectively capture the seasonal SM trend in this region, displaying a gradual drying from January to July, followed by increased moisture in October. The GLASS and DS-CCI data provide seamless daily SM estimates across both temporal and spatial dimensions, making them highly useful for analyzing spatiotemporal SM variability on regional and global scales. However, both products rely on machine leaning algorithms, which are limited in explaining the radiative transfer mechanism. In both data products, NDVI was identified as a significant input parameter, yielding highly similar distribution patterns for SM and NDVI, as shown in the second and third lines of Fig. 7.

The DS-SMAP product downscales the 9 km SMAP SM product (SPL2SMP_E) to a 1 km resolution by leveraging the negative correlation between SM and land surface temperature changes under a given vegetation cover. This product retains the 100 km swath width and 1–2 day revisit period of the SMAP passive microwave radiometer, giving it an advantage over the S1-DPA product in temporal coverage. However, despite being grounded in physical principles, the coarse-resolution pixel decomposition algorithm employed may introduce discontinuities in the 1 km results, particularly at the edges of the 9 km cells. This

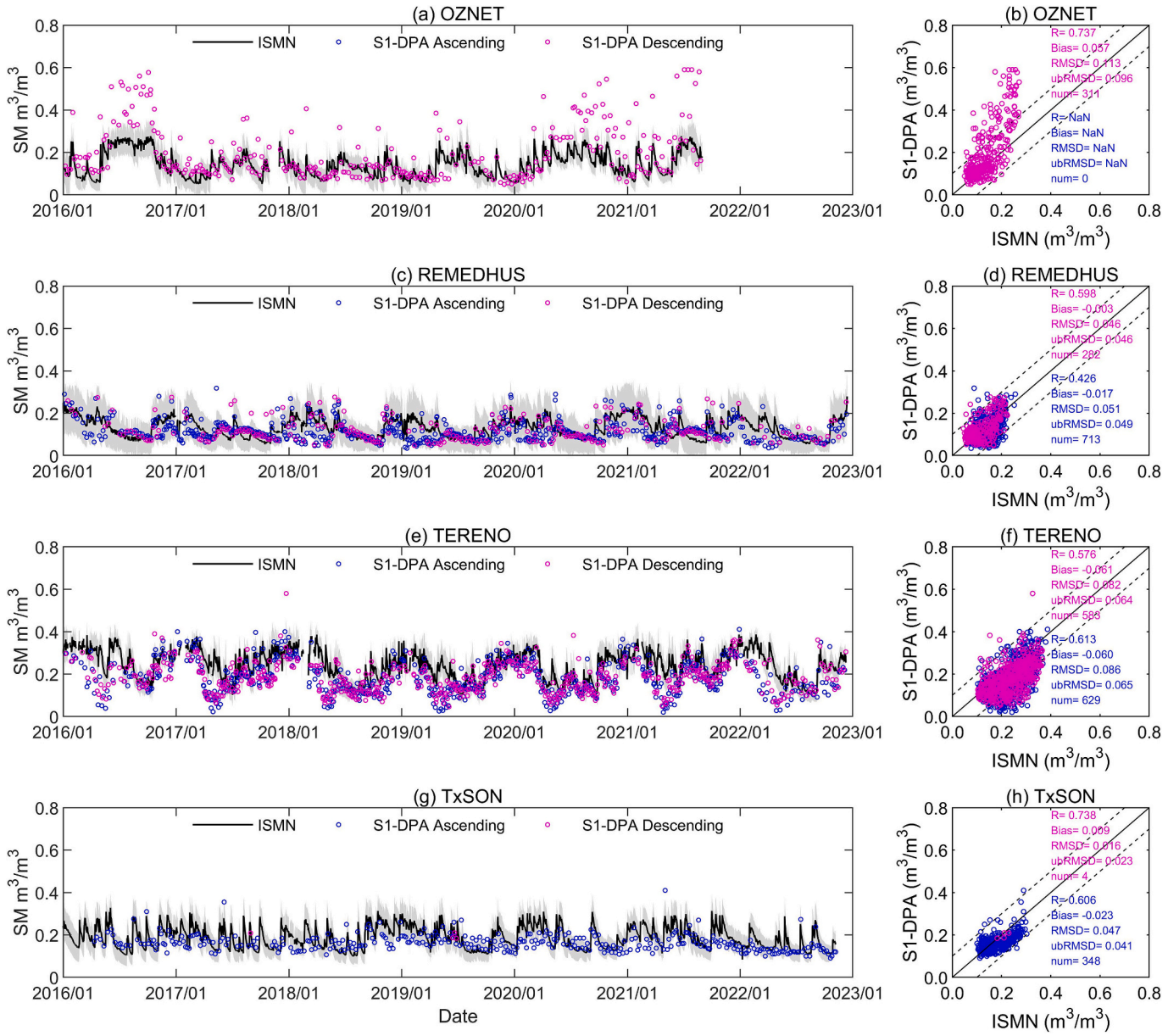

Fig. 4. Temporal variations of the SM derived from S1-DPA and ISMN during 2016–2022: OZNET (a, b), REMEDHUS (c, d), TERENO (e, f), and TxSON (g, h). Data from ascending orbits are shown as blue dots and data from descending orbits as pink dots, while the black lines denote the average of the SM from ISMN and the gray area is the $\mu \pm \sigma$. The dotted lines in the scatter plots indicate the margin of ± 0.1 m^3/m^3. (For interpretation of the references to colour in this figure legend, the reader is referred to the web version of this article.)

issue, known as the "block effect", is more pronounced in regions with high spatial variability in SM, as illustrated in the fourth line of Fig. 7.

The SPL2SMAP_S product utilizes 1-km-resolution Sentinel-1 SAR backscatter to capture the spatial heterogeneity within the 9-km SMAP microwave radiometer pixels. This method enables the downscaling of coarse-resolution brightness temperatures to finer resolutions, followed by inversion to produce SM data at a 1-km resolution. By relying exclusively on active and passive microwave remote sensing observations, the product provides a detailed representation of SM's spatial distribution, as illustrated in the fifth line of Fig. 7. However, this approach requires concurrent observations from both the SMAP microwave radiometer and Sentinel-1 SAR, resulting in a lower temporal resolution compared to the S1-DPA product, as shown in Appendix C.

Fig. 8 illustrates the R values, bias, RMSD, and ubRMSD for the five SM products across all available ISMN sites in 2020. These sites are primarily situated in woody savannas, savannas, grasslands, and croplands, with annual NDVI values ranging from 0.3 to 0.6. The GLASS and DS-CCI products, derived from machine learning and reanalysis data, demonstrate strong agreement with ground-based SM measurements. However, some ISMN-based SM measurements are used in model training, potentially inflating validation accuracy, as it is not possible within this study to determine which sites were included in training. Additionally, these products rely on reanalysis data, which may limit their ability to capture seasonal variations at high latitudes and represent fine-scale spatial changes in SM (Fig. 5 and Fig. 7). The DS-SMAP product maintains the high accuracy of passive microwave measurements and shows strong consistency with ground-based SM, making it an excellent source of SM data once the block effect is reduced. Comparing the SPL2SMAP_S and S1-DPA products, both of which utilize Sentinel-1 SAR, SPL2SMAP_S demonstrates relatively higher accuracy when NDVI is below 0.5, while S1-DPA outperforms it when NDVI exceeds 0.5.

Overall, the S1-DPA product developed in this study exhibits lower

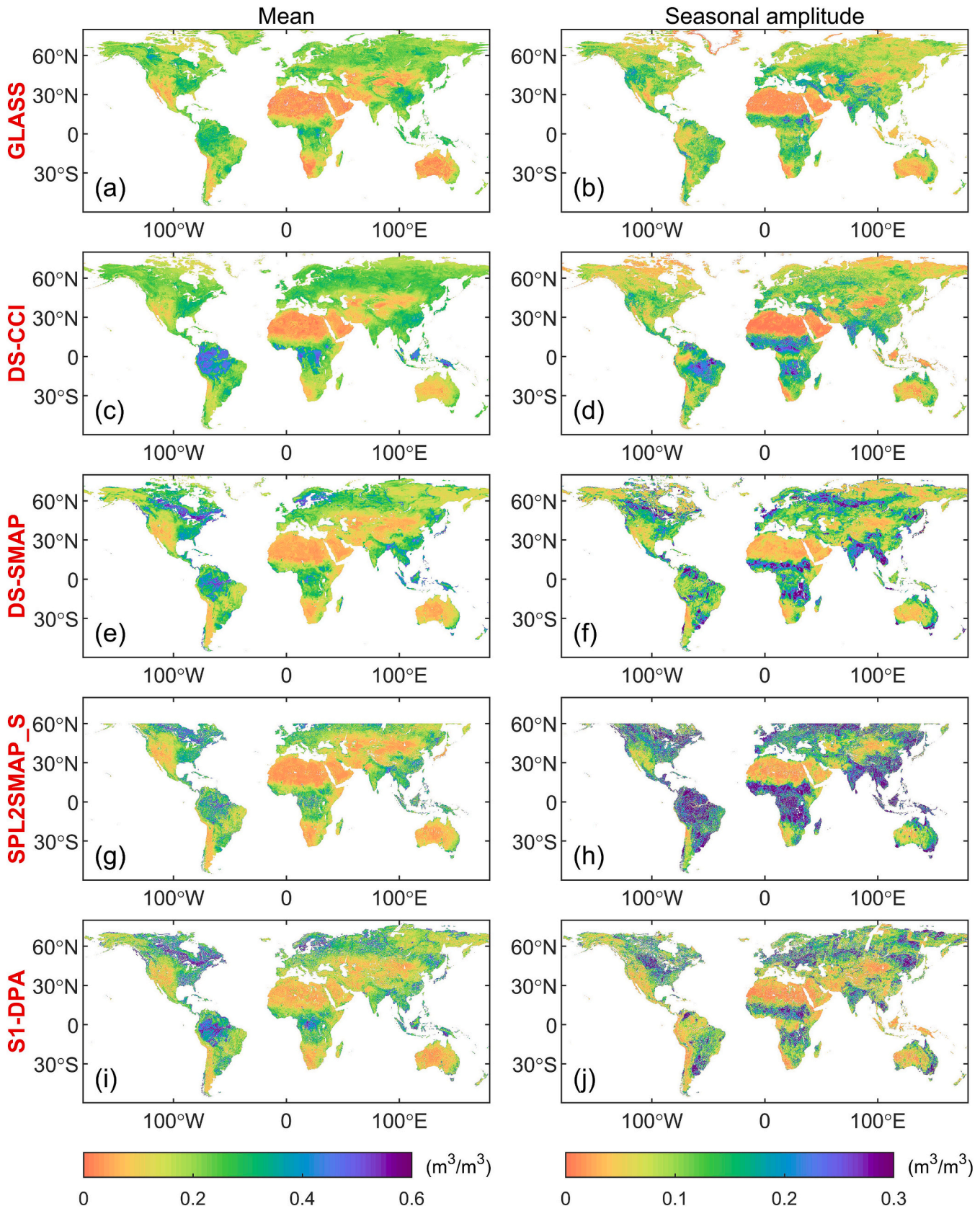

Fig. 5. Global pattern of the temporal average and annual seasonal amplitude of different global SM products with 1 km resolution for 2020: GLASS (a, b), DS-CCI (c, d), DS-SMAP (e, f), SPL2SMAP_S (g, h) and S1-DPA (i, j).

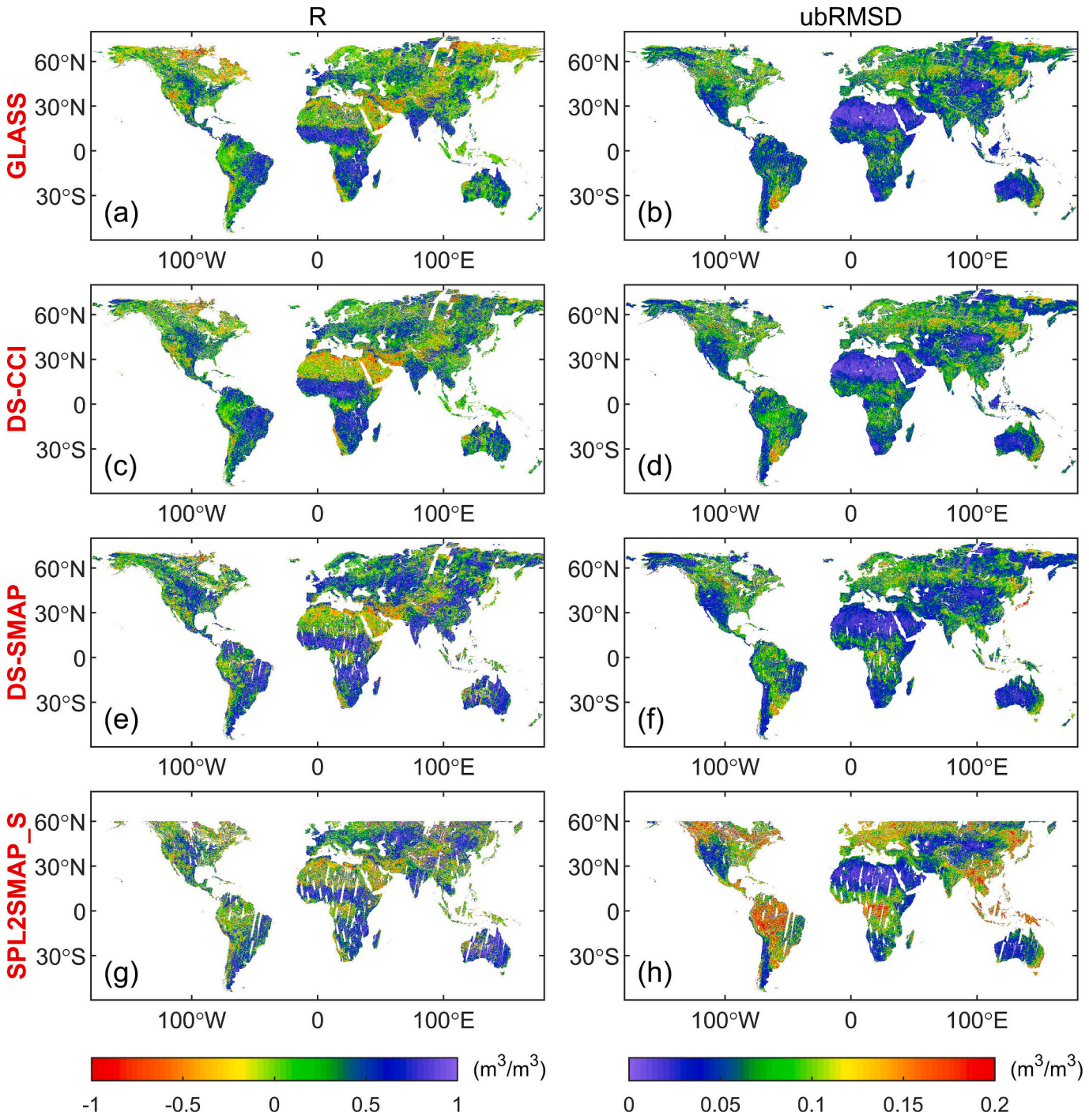

Fig. 6. Spatial pattern of correlation coefficients (R) and unbiased root-mean-square differences (ubRMSD) for the S1-DPA compared with GLASS (a, b), DS-CCI (c, d), DS-SMAP (e, f) and SPL2SMAP_S (g, h) in 2020.

accuracy than the GLASS and DS-CCI products, which rely on reanalysis and machine learning. Nevertheless, S1-DPA excels in capturing the spatiotemporal details of SM. Compared to DS-SMAP, which is based on passive microwave product decomposition, S1-DPA exhibits lower accuracy but offers superior spatial continuity without noticeable block effects. When compared to the SPL2SMAP_S product, which also utilizes Sentinel-1 data, S1-DPA achieves slightly higher accuracy at higher NDVI values and provides better temporal resolution.

5. Discussion

5.1. Effect of land cover on retrieval accuracy

Both the soil and vegetation scattering models used in this study are semi-empirical, which have the advantage of requiring only a few input parameters. However, the Oh model is not adjusted for the scattering of the subsurface soil, and the accuracy of the backscatter simulation is limited over highly rough surfaces (Oh et al., 1992). Therefore, it may not be suitable for areas with extremely low SM and high roughness. The water-cloud model, which interprets vegetation as a horizontally

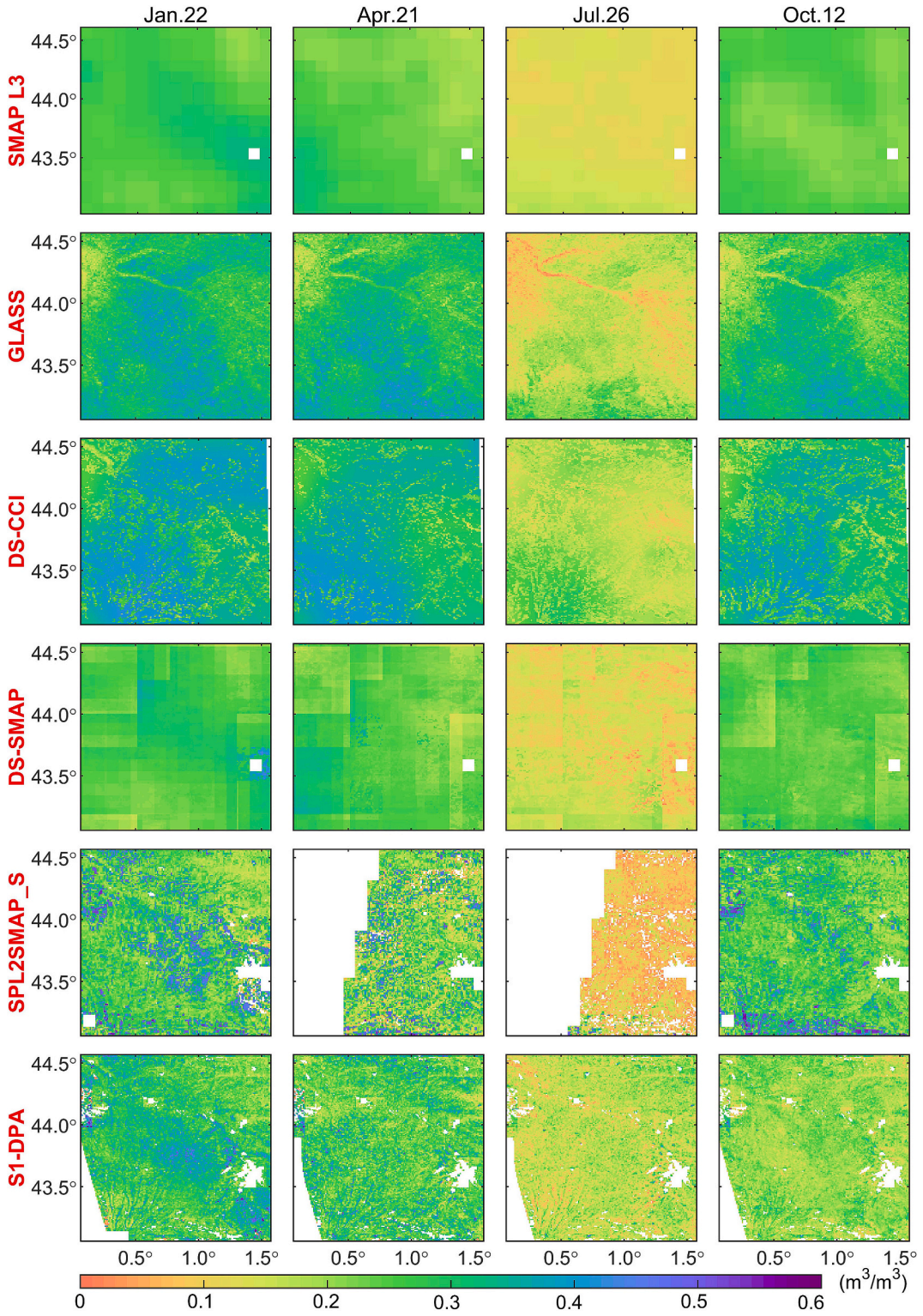

Fig. 7. Spatiotemporal patterns of SM around the SMOSMANIA network on January 22, April 21, July 26, and October 12, 2020, for six SM products. The first row presents data at a spatial resolution of 9 km, while the remaining rows display data at a 1-km resolution. White pixels denote observation strip gaps or areas unsuitable for SM retrieval.

uniform scatter, ignores the multiple scattering between the vegetation layer and the soil surface. This simplification can be justified in areas such as grasslands, but the applicability of this model may be reduced in areas with high vegetation (Wang et al., 2023).

As shown in Table 5, the S1-DPA product exhibits higher accuracy in croplands (C), grasslands (G), and cropland/natural vegetation mosaics (CNVM), while demonstrating lower accuracy in dense forests (ENF, EBF, and DBF) and barren or sparsely vegetated regions (B). For land cover types such as grasslands, their vegetation characteristics align with the assumptions in the water-cloud model employed by this algorithm. This enables the forward model to accurately describe the transmission process of SAR signals in this type of vegetation, resulting

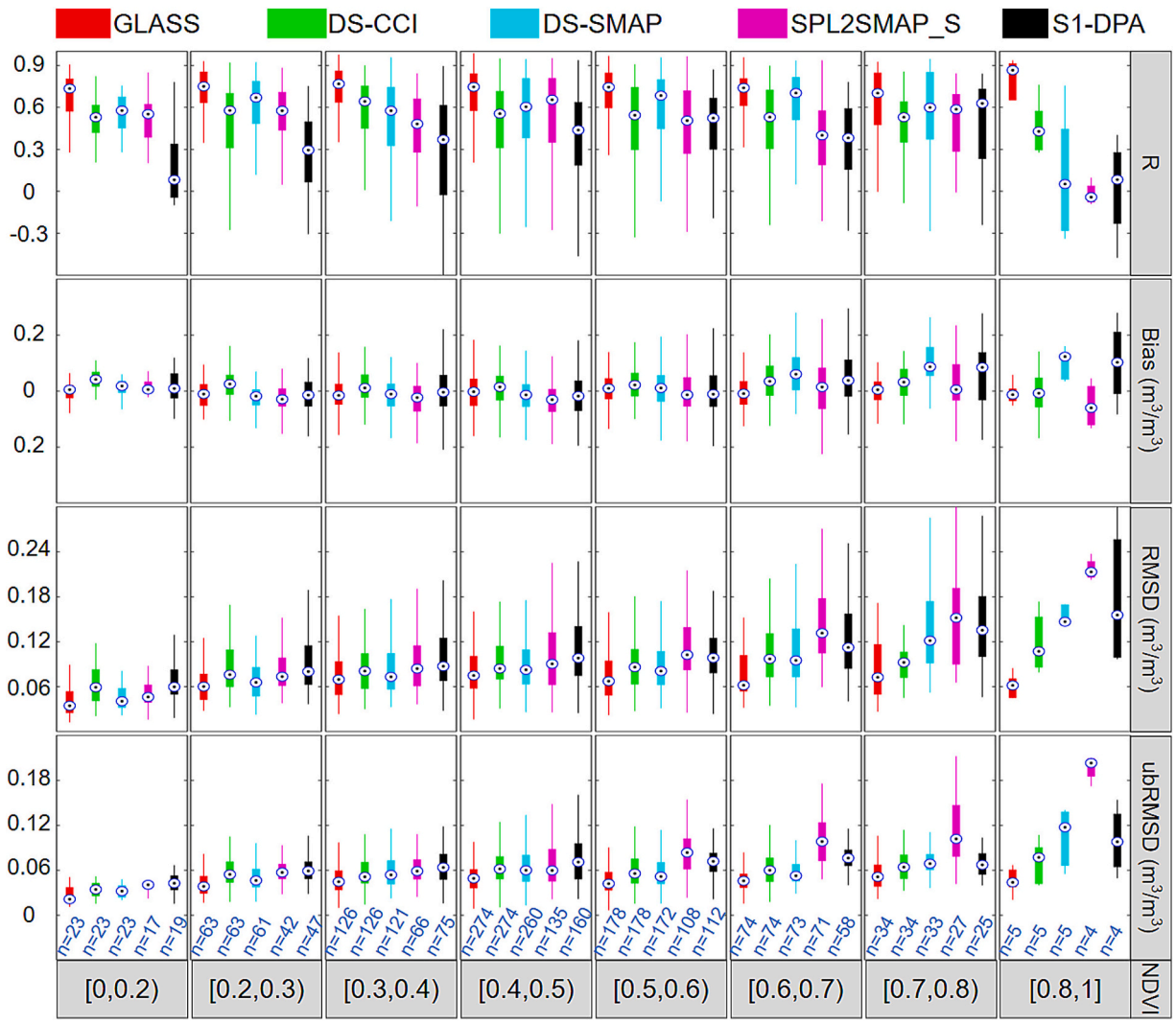

Fig. 8. Boxplots of the five SM products across different NDVI levels in 2020. The median values are indicated by points within the boxplots, while the box edges represent the 25th and 75th percentiles. The numbers below the boxplots denote the count of sites included in the analysis, excluding those with fewer than 10 valid data pairs.

Table 5
Comparison between the S1-DPA and ISMN over different land cover types from 2016 to 2022. The land cover type is obtained from MODIS data in 2020, aggregated by mode to a resolution of 1 km. The majority of stations are located at grasslands, croplands, and savannas.

IGBP	Median R	Median Bias (m^3/m^3)	Median RMSD (m^3/m^3)	Median ubRMSD (m^3/m^3)	Number of Stations	Data pairs
ENF	0.140	0.100	0.145	0.097	33	5060
EBF	0.066	−0.086	0.125	0.076	4	433
DBF	0.306	0.116	0.161	0.099	17	1863
MF	0.409	0.115	0.154	0.083	6	1733
CS	0.401	−0.026	0.080	0.075	2	761
OS	0.313	0.013	0.070	0.042	43	7575
WS	0.307	0.047	0.122	0.076	115	17,372
S	0.340	0.002	0.110	0.079	198	37,443
G	0.414	−0.016	0.094	0.071	545	60,189
C	0.419	−0.006	0.123	0.095	296	57,783
CNVM	0.550	0.001	0.099	0.089	19	6897
B	0.127	0.001	0.056	0.035	21	1778

in higher SM estimation accuracy compared to other land cover types. In contrast, for forests, scattering from trunks and interaction scattering from the vegetation canopy to the soil surface are not accounted for in the water-cloud model. Additionally, the penetration of C-band radar into dense vegetation, such as forests, still presents significant uncertainty, leading to low product accuracy in forested areas. In barren or sparsely vegetated regions, the penetration effect of microwaves and the structure of the subsurface soil can result in a negative correlation between SM and backscattering, as noted by Ullmann et al. (2023).

Fig. 9 illustrates the spatial distribution of statistical parameters for the S1-DPA product at each ground observation site. At most sites, a positive correlation is observed between S1-DPA and in situ SM measurements. However, a negative correlation is noted between S1-DPA and ISMN data in the CONUS region (Fig. 9b), including sites such as FordDryLake, DesertCenter, DeathValleyJCT, and TuleValley from the SCAN network; ANGUS-PROP and IMPS-SCGN from the PBO_H2O network; and Stovepipe-Wells-1-SW from the USCRN network. These sites, classified as barren in the MODIS IGBP dataset, align with the statistical results presented in Table 5. Other validation indicators reveal that regions with larger errors are primarily situated in the mountainous areas of the western and eastern United States, where terrain and vegetation conditions are more complex compared to the central plains.

5.2. *Effect of terrain on retrieval accuracy*

Terrain induces variations in the SAR backscattering coefficient by

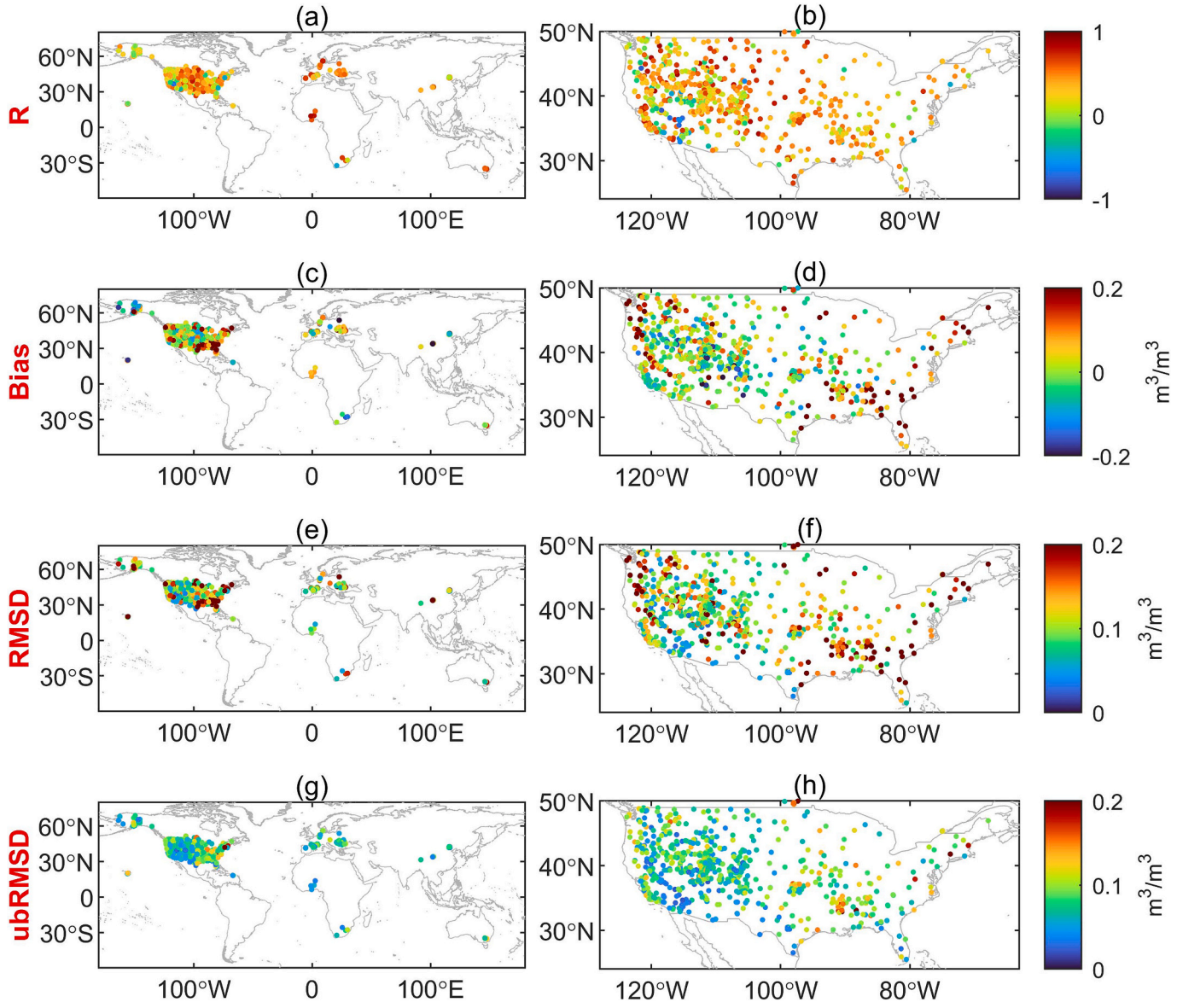

Fig. 9. Statistical values between S1-DPA and ISMN data over all sites in the global (left) and the continental United States (right) during 2016–2022: R (a, b), bias (c, d), RMSD (e, f), and ubRMSD (g, h).

affecting the local incidence angle. In this study, we applied the LIA-based backscatter normalization method proposed by Bauer-Marschallinger et al. (2021) to reduce terrain effects on the backscattering coefficient (see Eq. 2). This method uses a linear correction approach to normalize backscatter in mountainous regions, offering advantages such as fewer input parameters and higher computational efficiency. However, it is important to note that the parameters in this method are derived from long-term backscattering coefficient time series within Europe, and their validity has not been widely tested outside this region. Additionally, the method uses the same correction parameters for both VV and VH polarizations, without accounting for differences in backscattering polarization effects across varying LIAs.

Fig. 10 shows that as slope increases, the R decreases, while bias, RMSD, and ubRMSD between S1-DPA and ISMN data increase. For sites with slopes between 0 and 15 degrees, SM retrieval accuracy shows minimal variation with slope. However, accuracy notably declines for slopes above 15 degrees. Additionally, under relatively gentle slopes, SM retrieval accuracy is similar for both ascending and descending observations when the same correction coefficients are applied (see Eq. 2). This finding indirectly supports the effectiveness of the LIA-based backscatter normalization method proposed by Bauer-Marschallinger et al. (2021) in areas with gentle slopes, regardless of orbit direction and extending beyond Europe.

5.3. *Effect of vegetation water content on retrieval accuracy*

This study utilizes climatologically processed global MODIS NDVI data, combined with MODIS land cover data, to estimate VWC on a grid-by-grid basis, similar to the SMAP single-channel algorithm. This approach addresses the limitations of optical bands, which are sensitive to clouds and precipitation, by providing a temporally and spatially continuous vegetation dataset. However, since these data represent a theoretical value for each pixel on a specific day of the year, they may not accurately capture the vegetation state at the time of a Sentinel-1 overpass. Consequently, the accuracy of the S1-DPA product may decrease in cases of abrupt vegetation or land cover changes, such as those caused by extreme events like droughts or floods.

To investigate the dependence of the algorithm on vegetation, we calculated the mean values of VWC at each site and assessed the accuracy of S1-DPA at different VWC levels (Fig. 11). The mean VWC values

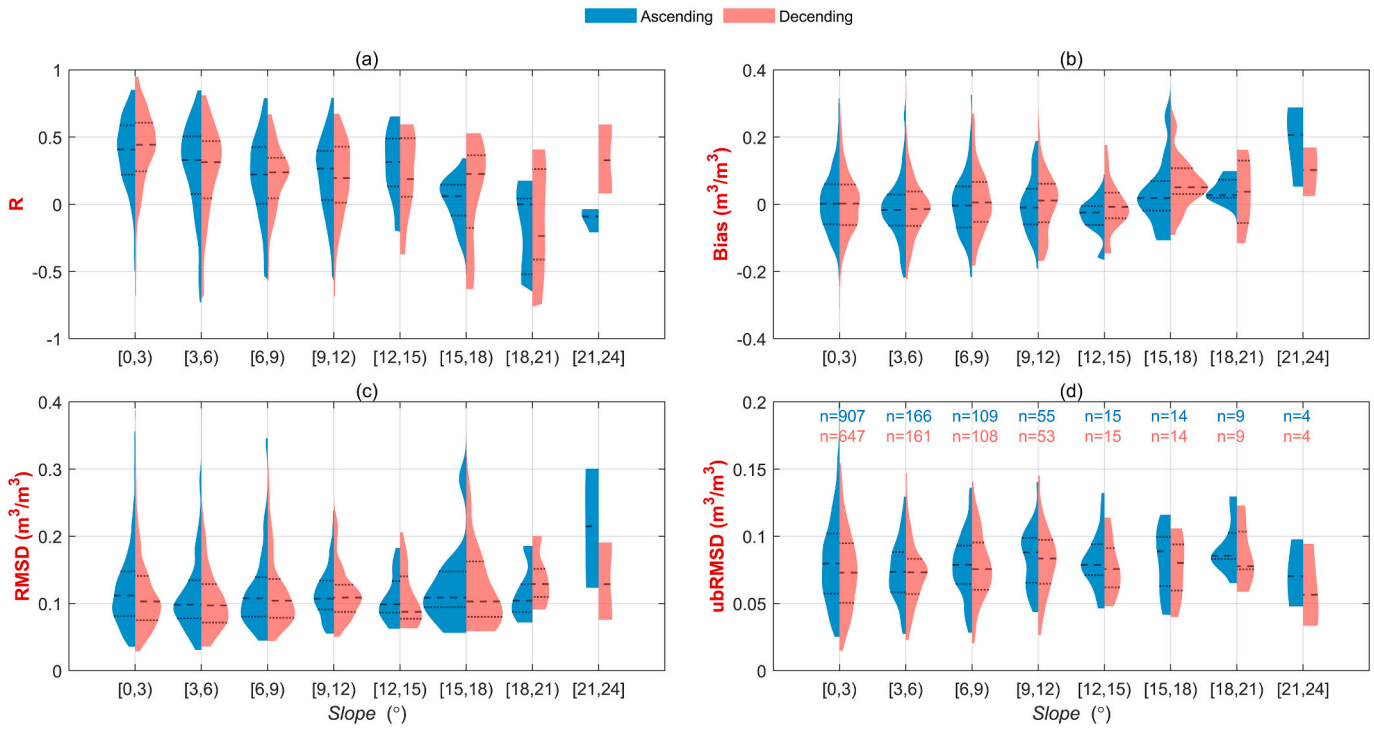

Fig. 10. Statistical values of R, bias, RMSD, and ubRMSD divided by different slope gradients for S1-DPA at all ISMN sites during 2016–2022.

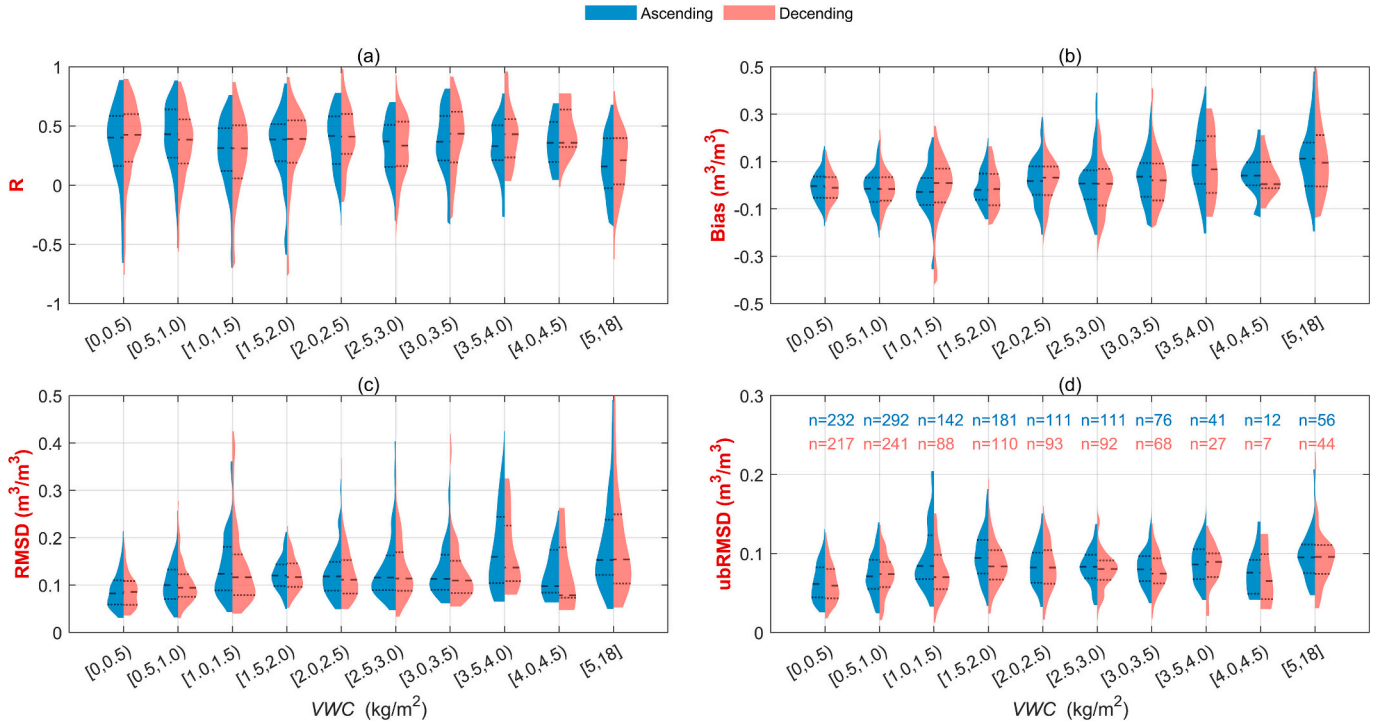

Fig. 11. Statistical values of R, bias, RMSD, and ubRMSD divided by various VWC levels for S1-DPA at all ISMN sites during 2016–2022.

across all sites range from 0 kg/m^2 to 17.8 kg/m^2. These values can be categorized into two subsets: sites in forested areas with VWC greater than 10.2 kg/m^2, and most other sites with VWC less than 4.3 kg/m^2. Fig. 11 shows that for VWC less than 4.5 kg/m^2, the error in S1-DPA data slightly increases with higher VWC, though the variation remains limited, with unbiased root-mean-square difference (ubRMSD) generally below 0.1 m^3/m^3 for most sites. However, in areas where VWC exceeds 5.0 kg/m^2, extremely high VWC levels complicate soil moisture retrieval, leading to reduced accuracy of the S1-DPA product.

5.4. *Effect of precipitation and priori SM data on retrieval accuracy*

The influence of precipitation is not accounted for in the proposed algorithm, which may lead to unreliable SM estimates under

precipitation conditions. To enhance the accuracy of the S1-DPA algorithm, pixels and conditions are excluded from the analysis if the cost function (Eq. 21) does not converge to an appropriate minimum during the SM retrieval process.

In the forward model, three parameters that vary with wavelength and land cover need to be pre-calibrated. In this study, the widely verified SMAP L3_SM_P_E product is used to pre-calibrate the vegetation parameters and surface roughness parameters in advance. It is noted that the contribution of vegetation cover and surface roughness to backscattering may even exceed that of SM in some cases. Therefore, there is a trade-off in calibrating these parameters in advance with long-term SM data. However, these parameters can be effectively calibrated using at least one year of SM data, allowing the calibrated forward model to be used independently for SAR-based SM retrieval.

6. Summary and conclusions

A semi-empirical forward model was developed by integrating the water-cloud model, the Oh model, and the Mironov model to simulate *V*V and VH backscatter across a range of SM and vegetation conditions. Three parameters of the forward model were calibrated for each 9 km grid cell globally, using the SMAP passive SM product for its high accuracy and spatiotemporal resolution. With these calibrated parameters, we proposed a backscatter cost function incorporating roughness constraints to estimate SM from Sentinel-1 dual-polarization SAR observations. As a result, a global SM product with a spatial resolution of 1 km was generated for the period from 2016 to 2022. *V*alidation was performed using ground-based measurements, followed by an analysis of factors affecting retrieval accuracy. The primary findings are summarized as follows.

The S1-DPA product effectively captures the spatiotemporal variation of SM. *V*alidation against SM data derived from 26 ground-based networks spanning 2016 to 2022 yielded a median correlation coefficient of 0.377, a bias of $-0.003\ m^3/m^3$, a RMSD of $0.105\ m^3/m^3$, and an ubRMSD of $0.077\ m^3/m^3$. The accuracy of SM estimation is higher in croplands, grasslands, and cropland/natural vegetation mosaics. Stations with significant errors are primarily located in deserts, forests, and areas with steep slopes, where SM retrieval is challenging due to the considerable and complex influence of land surface properties (e.g., vegetation and terrain) on the total observed backscatter signal.

The primary advantages of this newly developed dual-polarization algorithm are as follows: it requires only a single snapshot input of dual-polarization SAR data, making it suitable for large-scale SM mapping. The first global SM dataset at 1 km resolution based on Sentinel-1C-SAR has been produced. It offers daily ascending and descending SM estimates with a swath width of 250 km and a temporal resolution of 3–6 days in Europe and 6–12 days in other regions.

The primary limitations of the proposed algorithm are as follows: it requires external SM and vegetation data for pre-calibration of the forward model. Additionally, the forward model has limited capability to simulate volume scattering, multiple scattering, extremely rough surfaces, and lacks accuracy in deserts and areas with dense vegetation. The algorithm also does not account for the effect of precipitation.

CRediT authorship contribution statement

Dong Fan: Writing – original draft, Visualization, Validation, Software, Methodology, Investigation, Formal analysis, Data curation. **Tianjie Zhao:** Writing – review & editing, Resources, Formal analysis. **Xiaoguang Jiang:** Writing – review & editing, Supervision, Formal analysis. **Almudena García-García:** Writing – review & editing, Resources. **Toni Schmidt:** Writing – review & editing, Validation. **Luis Samaniego:** Writing – review & editing. **Sabine Attinger:** Writing – review & editing, Investigation. **Hua Wu:** Writing – review & editing, Resources. **Yazhen Jiang:** Writing – review & editing, Resources. **Jiancheng Shi:** Methodology, Formal analysis. **Lei Fan:** Writing – review & editing, Methodology. **Bo-Hui Tang:** Writing – review & editing, Supervision. **Wolfgang Wagner:** Writing – review & editing, Methodology, Formal analysis. **Wouter Dorigo:** Writing – review & editing, Resources, Data curation. **Alexander Gruber:** Writing – review & editing. **Francesco Mattia:** Writing – review & editing. **Anna Balenzano:** Writing – review & editing. **Luca Brocca:** Writing – review & editing. **Thomas Jagdhuber:** Writing – review & editing. **Jean-Pierre Wigneron:** Writing – review & editing, Methodology. **Carsten Montzka:** Writing – review & editing. **Jian Peng:** Writing – review & editing, Supervision, Resources, Project administration, Methodology, Funding acquisition, Formal analysis, Conceptualization.

Declaration of competing interest

The authors declare that they have no known competing financial interests or personal relationships that could have appeared to influence the work reported in this paper.

Acknowledgments

We express our gratitude to all organizations and institutions that provided data and support for this study. We sincerely thank the EC and ESA teams for providing Sentinel-1 SAR data. We also acknowledge NASA for the provision of MODIS NDVI, LULC, and SMAP SM data. Our thanks go to OpenLandMap for supplying soil texture data and to ECMWF for the ERA5-LAND temperature and snow cover data. We further extend our appreciation to ISMN for providing in situ SM observations and to the researchers who contributed open-source 1 km resolution global SM datasets. We acknowledge the technical support of the UFZ-IT team for the use of the EVE HPC server and and Google for providing the GEE platform.

This work was supported by the China Scholarsip Councial (No. 202004910767), ESA 4DHydro project (No. ESA AO/1-11298/22/I-EF), Helmholtz MoDE*V* project, ESA CLIMATE-Pan-TPE project, National Natural Science Foundation of China (NO. 42401464, 42090014), and Yunnan Fundamental Research Projects (NO. 202401CF070161).

Appendix A. Detailed equations for the dielectric constant model used

The real ε' and the imaginary ε'' parts of the complex dielectric constant of bare sol are derived form the refractive index n_s and the normalized attenuation coefficient k_s:

$$\varepsilon' = {n_s}^2 - {k_s}^2; \qquad \varepsilon'' = 2n_s k_s \tag{A1}$$

$$n_s = \begin{cases} n_d + (n_b - 1)m_s, & m_s < m_{st} \\ n_d + (n_b - 1)m_{st} + (n_u - 1)(m_s - m_{st}), & m_s \geq m_{st} \end{cases} \tag{A2}$$

$$k_s = \begin{cases} k_d + (k_b - 1)m_s, & m_s < m_{st} \\ k_d + (k_b - 1)m_{st} + (k_u - 1)(m_s - m_{st}), & m_s \geq m_{st} \end{cases} \tag{A3}$$

Where n_d and k_d are function of clay portion, n_b, k_b, n_u, and k_u can be calculated using the Debye relaxation equations:

$$n_{d,b,u}\sqrt{2} = \sqrt{\sqrt{\varepsilon'^{\,2}_{d,b,u} + \varepsilon''^{\,2}_{d,b,u}} + \varepsilon'_{d,b,u}} \tag{A4}$$

$$k_{d,b,u}\sqrt{2} = \sqrt{\sqrt{\varepsilon'^{\,2}_{d,b,u} + \varepsilon''^{\,2}_{d,b,u}} - \varepsilon'_{d,b,u}} \tag{A5}$$

$$\varepsilon'_{b,u} = \varepsilon_\infty + \frac{\varepsilon_{0b,0u} - \varepsilon_\infty}{1 + (2\pi f \tau_{b,u})^2} \tag{A6}$$

$$\varepsilon''_{b,u} = \frac{\varepsilon_{0b,0u} - \varepsilon_\infty}{1 + (2\pi f \tau_{b,u})^2} \cdot 2\pi f \tau_{b,u} + \frac{\sigma_{b,u}}{2\pi \varepsilon_0 f} \tag{A7}$$

The subscripts s, d, b, and u is the moist soil, dry soil, bound soil water and free soil water. The value f is the frequency of microware, τ is the relaxation time, ε_0 denotes the dielectric constant of free space, while ε_∞ represents the dielectric constant in the high-frequency limit. These parameters were fitted as a function of soil clay fraction (C) in the study of Mironov et al. (2009).

$$n_d = 1.634 - 0.539 \times 10^{-2} C + 0.2748 \times 10^{-4} C^2 \tag{A8}$$

$$k_d = 0.03952 - 0.04038 \times 10^{-2} C \tag{A9}$$

$$m_{st} = 0.02863 - 0.30673 \times 10^{-2} C \tag{A10}$$

$$\varepsilon_{0b} = 79.8 - 85.4 \times 10^{-2} C + 32.7 \times 10^{-4} C^2 \tag{A11}$$

$$\varepsilon_{0u} = 100 \tag{A12}$$

$$\tau_b = 1.062 \times 10^{-11} + 3.45 \times 10^{-14} C \tag{A13}$$

$$\tau_u = 8.5 \times 10^{-12} \tag{A14}$$

$$\sigma_b = 0.3112 + 0.467 \times 10^{-2} C \tag{A15}$$

$$\sigma_u = 0.3631 + 1.217 \times 10^{-2} C \tag{A16}$$

$$\varepsilon_0 = 8.854 \times 10^{-12} \tag{A17}$$

$$\varepsilon_\infty = 4.9 \tag{A18}$$

Appendix B. Forward model parameter calibration results and statistics

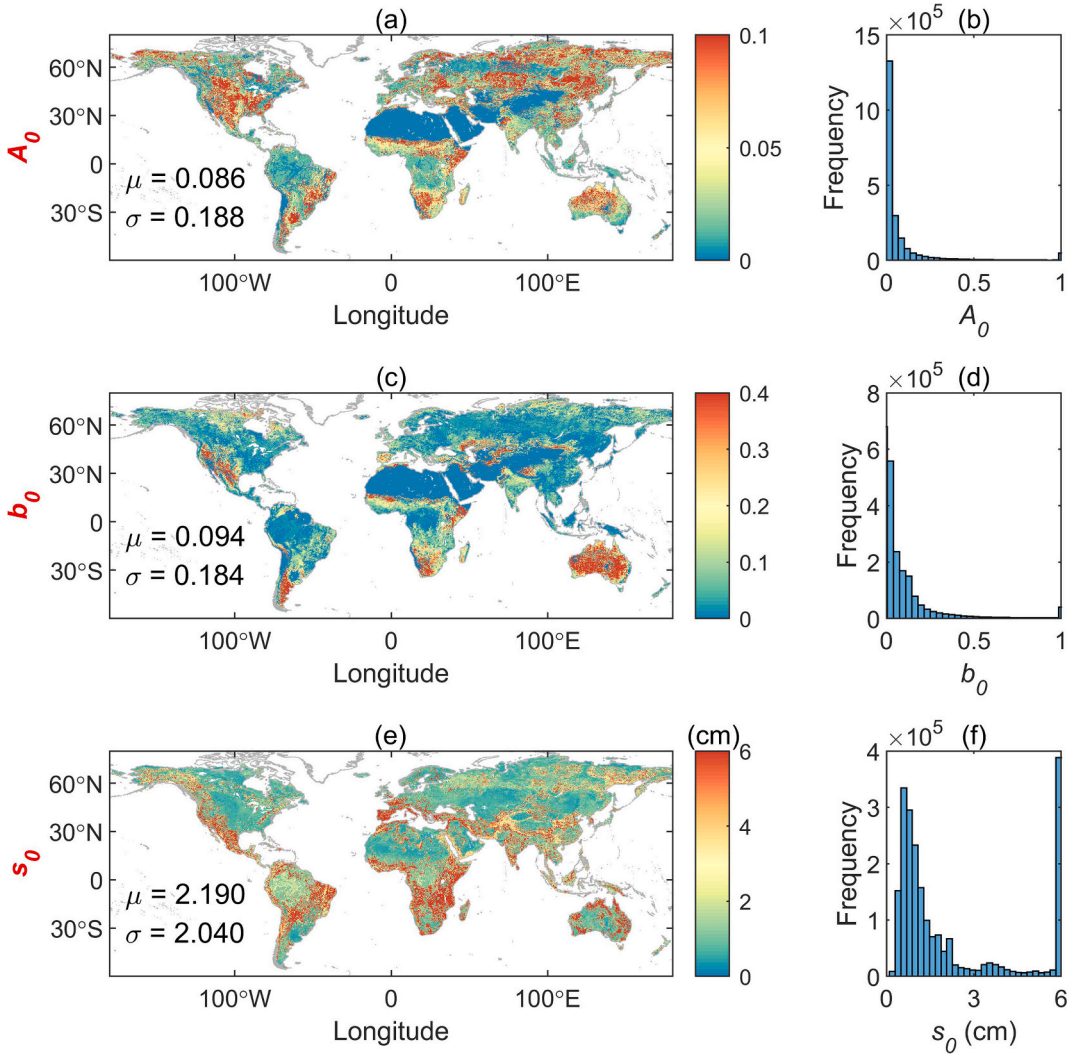

Fig. B1. Spatial pattern of the calibrated parameters A_0 (a), b_0 (b), and s_0 (c), while their means and standard deviations are denoted as μ and σ. The pixels marked as barren by MODIS IGBP are assumed to have no vegetation cover, and A_0 and b_0 are set to 0 in the calibration process.

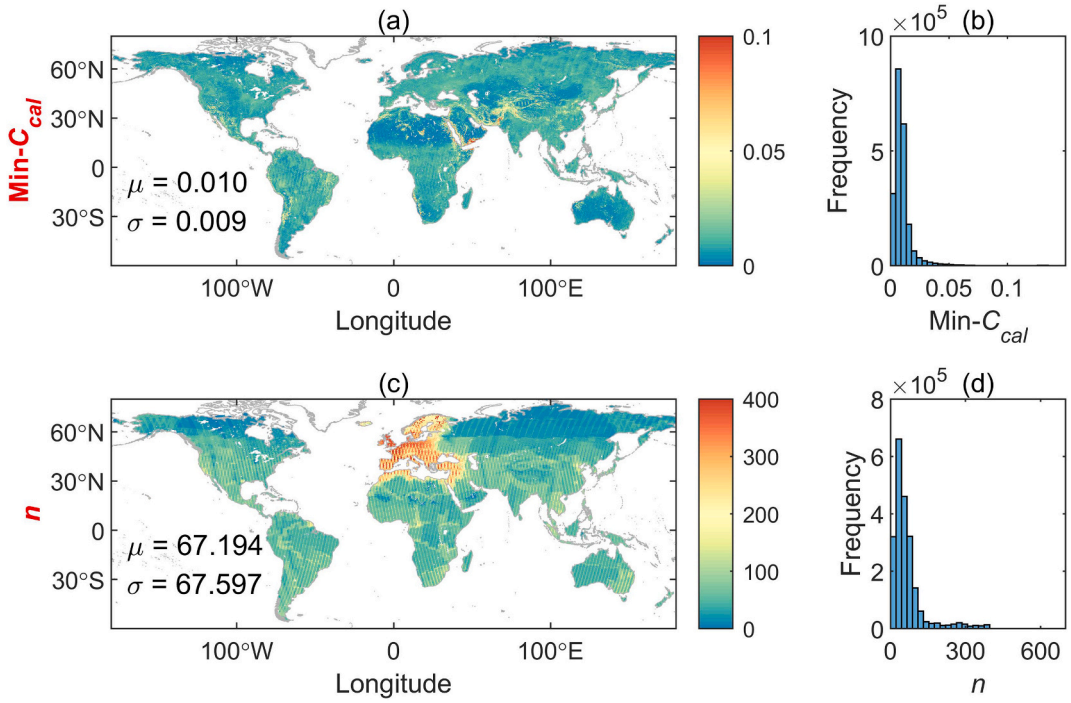

Fig. B2. The minimum of the cost function C_{cal} (a, b) and the effective data volume (c, d) involved in the forward model calibration. Their means and standard deviations are denoted as μ and σ, respectively. All data have a grid size of 9 km.

Table B1
Statistical values of the calibrated parameters for different land cover types.

IGBP	A_0		b_0		s_0 (cm)		Simulation error (linear)		Number of valid observations	
	mean	standard deviation	mean	standard deviation	mean	standard deviation	mean	standard deviation	mean	standard deviation
ENF	0.007	0.023	0.015	0.015	1.444	1.154	0.006	0.002	42.987	45.909
EBF	0.020	0.074	0.010	0.013	2.240	1.654	0.011	0.004	60.458	27.991
DNF	0.017	0.023	0.012	0.009	1.132	1.057	0.005	0.001	14.393	6.849
DBF	0.042	0.113	0.014	0.013	2.290	1.810	0.009	0.003	61.329	52.035
MF	0.017	0.052	0.011	0.009	1.131	1.024	0.006	0.002	29.650	35.745
CS	0.039	0.062	0.285	0.238	3.769	1.921	0.006	0.005	44.978	21.768
OS	0.072	0.122	0.206	0.298	1.434	1.693	0.004	0.003	30.631	35.232
WS	0.050	0.084	0.022	0.026	1.416	1.631	0.006	0.003	37.361	37.461
S	0.053	0.107	0.047	0.053	2.241	2.149	0.007	0.004	43.228	43.830
G	0.095	0.173	0.141	0.179	1.784	1.928	0.007	0.004	47.905	36.830
PW	0.014	0.046	0.003	0.014	0.430	0.350	0.007	0.003	14.631	15.594
C	0.133	0.231	0.051	0.056	1.541	1.691	0.009	0.003	80.388	64.614
U	–	–	–	–	–	–	–	–	–	–
CNVM	0.121	0.205	0.036	0.037	2.661	2.094	0.011	0.005	80.153	52.368
PSI	–	–	–	–	–	–	–	–	–	–
B	–	–	–	–	1.510	1.599	0.005	0.004	59.895	42.195
W	–	–	–	–	–	–	–	–	–	–

Appendix C. Effective data of SPL2SMAP_S and S1-DPA in 2020

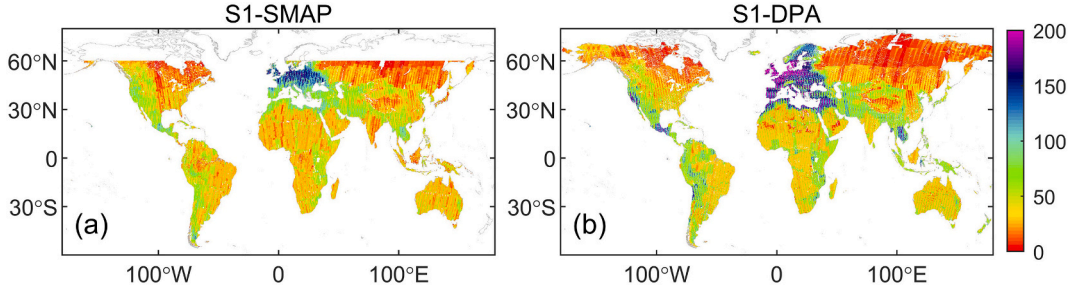

Fig. C1. The number of effective data in 2020 for two global 1-km resolution SM products involving Sentinel-1 SAR: SPL2SMAP_S (a) and S1-DPA (b).

Data availability

Sentinel-1 DPA data will be available on this website: https://doi.pangaea.de/10.1594/PANGAEA.968754

References

Al Bitar, A., Mialon, A., Kerr, Y., Cabot, F., Richaume, P., Jacquette, E., Quesney, A., Mahmoodi, A., Tarot, S., Parrens, M., Al-Yaari, A., Pellarin, T., Rodriguez-Fernandez, N., Wigneron, J., 2017. The global SMOS level 3 daily soil moisture and brightness temperature maps. Earth Syst. Sci. Data 9, 293–315.

Albergel, C., Ruediger, C., Pellarin, T., Calvet, J., Fritz, N., Froissard, F., Suquia, D., Petitpa, A., Piguet, B., Martin, E., 2008. From near-surface to root-zone soil moisture using an exponential filter: an assessment of the method based on in-situ observations and model simulations. Hydrol. Earth Syst. Sci. 12, 1323–1337.

Al-Yaari, A., Dayau, S., Chipeaux, C., Aluome, C., Kruszewski, A., Loustau, D., Wigneron, J.P., 2018. The AQUI soil moisture network for satellite microwave remote sensing validation in South-Western France. Remote Sens. 10, 123–139.

Attema, E., Ulaby, F., 1978. Vegetation modeled as a water cloud. Radio Sci. 13, 357–364.

Attema, E., Cafforio, C., Gottwald, M., Guccione, P., Monti Guarnieri, A., Rocca, F., Snoeij, P., 2010. Flexible dynamic block adaptive quantization for Sentinel-1 SAR missions. IEEE Geosci. Remote Sens. Lett. 7, 766–770.

Baatz, R., Hendricks Franssen, H., Euskirchen, E., Sihi, D., Dietze, M., Ciavatta, S., Fennel, K., Beck, H., De Lannoy, G., Pauwels, V.R.N., Raiho, A., Montzka, C., Williams, M., Mishra, U., Poppe, C., Zacharias, S., Lausch, A., Samaniego, L., Van Looy, K., Bogena, H., Adamescu, M., Mirtl, M., Fox, A., Goergen, K., Naz, B.S., Zeng, Y., Vereecken, H., 2021. Reanalysis in earth system science: toward terrestrial ecosystem reanalysis. Rev. Geophys. 59.

Babaeian, E., Sadeghi, M., Jones, S., Montzka, C., Vereecken, H., Tuller, M., 2019. Ground, proximal, and satellite remote sensing of soil moisture. Rev. Geophys. 57, 530–616.

Balenzano, A., Mattia, F., Satalino, G., Lovergine, F.P., Palmisano, D., Peng, J., Marzahn, P., Wegmüller, U., Cartus, O., Dąbrowska-Zielińska, K., Musial, J., Davidson, M., Pauwels, V., Cosh, M., McNairn, H., Johnson, J., Walker, J., Yueh, S., Entekhabi, D., Kerr, Y., Jackson, T., 2021. Sentinel-1 soil moisture at 1 km resolution: a validation study. Remote Sens. Environ. 263, 112554.

Bauer-Marschallinger, B., Freeman, V., Cao, S., Paulik, C., Schaufler, S., Stachl, T., Modanesi, S., Massari, C., Ciabatta, L., Brocca, L., Wagner, W., 2019. Toward global soil moisture monitoring with Sentinel-1: harnessing assets and overcoming obstacles. IEEE Trans. Geosci. Remote Sens. 57, 520–539.

Bartalis, Z., Wagner, W., Naeimi, V., Hasenauer, S., Scipal, K., Bonekamp, H., Figa, J., Anderson, C., 2007. Initial soil moisture retrievals from the METOP-a Advanced Scatterometer (ASCAT). Geophys. Res. Lett. 34.

Bauer-Marschallinger, B., Cao, S., Navacchi, C., Freeman, V., Reuß, F., Geudtner, D., Rommen, B., Vega, F.C., Snoeij, P., Attema, E., Reimer, C., Wagner, W., 2021. The normalised Sentinel-1 global backscatter model, mapping Earth's land surface with C-band microwaves. Sci. Data 8, 1–18.

Beaudoing, H., Rodell, M., 2020. GLDAS Noah Land Surface Model L4 3 hourly 0.25 x 0.25 degree V2.1.

Beck, H., Pan, M., Miralles, D., Reichle, R., Dorigo, W., Hahn, S., Sheffield, J., Karthikeyan, L., Balsamo, G., Parinussa, R.M., van Dijk, A., Du, J., Kimball, J., Vergopolan, N., Wood, E., 2021. Evaluation of 18 satellite- and model-based soil moisture products using in situ measurements from 826 sensors. Hydrol. Earth Syst. Sci. 25, 17–40.

Bell, J., Palecki, M., Baker, C., Collins, W., Lawrimore, J., Leeper, R., Hall, M., Kochendorfer, J., Meyers, T., Wilson, T., Diamond, H., 2013. U.S. climate reference network soil moisture and temperature observations. J. Hydrometeorol. 14, 977–988.

Bindlish, R., Jackson, T., Zhao, T., 2011. A MODIS-Based Vegetation Index Climatology. SPIE, Bellingham WA, pp. 815603–815608.

Bindlish, R., Jackson, T., Cosh, M., Zhao, T., O'Neill, P., 2015. Global soil moisture from the Aquarius/SAC-D satellite: description and initial assessment. IEEE Geosci. Remote Sens. Lett. 12, 923–927.

Bloeschl, G., Blaschke, A., Broer, M., Bucher, C., Carr, G., Chen, X., Eder, A., Exner-Kittridge, M., Farnleitner, A., Flores-Orozco, A., Haas, P., Hogan, P., Amiri, A., Oismueller, M., Parajka, J., Silasari, R., Stadler, P., Strauss, P., Vreugdenhil, M., Wagner, W., Zessner, M., 2016. The hydrological open air laboratory (HOAL) in Petzenkirchen: a hypothesis-driven observatory. Hydrol. Earth Syst. Sci. 20, 227–255.

Boeing, F., Oldrich, R., Rohini, K., Luis, S., Martin, S., Anke, H., Corinna, R., 2022. High-resolution drought simulations and comparison to soil moisture observations in Germany. Hydrol. Earth Syst. Sci. 26, 5137–5161.

Chen, K., Wu, T., Tsang, L., Li, Q., Shi, J., Fung, A., 2003. Emission of rough surfaces calculated by the integral equation method with comparison to three-dimensional moment method simulations. IEEE Trans. Geosci. Remote Sens. 41, 90–101.

Caldwell, T., Bongiovanni, T., Cosh, M., Jackson, T., Colliander, A., Abolt, C., Casteel, R., Larson, T., Scanlon, B., Young, M., 2019. The texas soil observation network:a comprehensive soil moisture dataset for remote sensing and land surface model validation. Vadose Zone Journal 18, 1–20.

Chen, Y., Feng, X., Fu, B., 2021. An improved global remote-sensing-based surface soil moisture (RSSSM) dataset covering 2003–2018. Earth Syst. Sci. Data 13, 1–31.

Cook, D., 2016. Soil temperature and moisture profile (STAMP) system handbook. In: DOE Office of Science Atmospheric Radiation Measurement (ARM).

Danielson, J., Gesch, D., 2011. Global Multi-Resolution Terrain Elevation Data 2010 (GMTED2010): US Department of the Interior. US Geological Survey Washington, DC, USA.

Das, N., Entekhabi, D., Dunbar, R., Chaubell, M., Colliander, A., Yueh, S., Jagdhuber, T., Chen, F., Crow, W., O'Neill, P., Walker, J., Berg, A., Bosch, D., Caldwell, T., Cosh, M., Collins, C., Lopez-Baeza, E., Thibeault, M., 2019. The SMAP and Copernicus sentinel 1A/B microwave active-passive high resolution surface soil moisture product. Remote Sens. Environ. 233, 111380.

Dobson, M.C., Ulaby, F.T., Hallikainen, M.T., El-rayes, M.A., 1985. Microwave dielectric behavior of wet soil-part ii: dielectric mixing models. IEEE Trans. Geosci. Remote Sens. 23, 35–46.

Dorigo, W.A., Wagner, W., Hohensinn, R., Hahn, S., Paulik, C., Xaver, A., Gruber, A., Drusch, M., Mecklenburg, S., van Oevelen, P., Robock, A., Jackson, T., 2011. The international soil moisture network: a data hosting facility for global in situ soil moisture measurements. Hydrol. Earth Syst. Sci. 15, 1675–1698.

Dorigo, W., Wagner, W., Albergel, C., Albrecht, F., Balsamo, G., Brocca, L., Chung, D., Ertl, M., Forkel, M., Gruber, A., Haas, E., Hamer, P.D., Hirschi, M., Ikonen, J., de Jeu, R., Kidd, R., Lahoz, W., Liu, Y.Y., Miralles, D., Mistelbauer, T., Nicolai-Shaw, N., Parinussa, R., Pratola, C., Reimer, C., van der Schalie, R., Seneviratne, S.I., Smolander, T., Lecomte, P., 2017. ESA CCI soil moisture for improved earth system understanding: state-of-the art and future directions. Remote Sens. Environ. 203, 185–215.

Dorigo, W., Himmelbauer, I., Aberer, D., Schremmer, L., Petrakovic, I., Zappa, L., Preimesberger, W., Xaver, A., Annor, F., Ardö, J., Baldocchi, D., Bitelli, M., Blöschl, G., Bogena, H., Brocca, L., Calvet, J., Camarero, J.J., Capello, G., Choi, M., Cosh, M.C., van de Giesen, N., Hajdu, I., Ikonen, J., Jensen, K.H., Kanniah, K.D., de Kat, I., Kirchengast, G., Kumar Rai, P., Kyrouac, J., Larson, K., Liu, S., Loew, A., Moghaddam, M., Martínez Fernández, J., Mattar Bader, C., Morbidelli, R., Musial, J. P., Osenga, E., Palecki, M.A., Pellarin, T., Petropoulos, G.P., Pfeil, I., Powers, J., Robock, A., Rüdiger, C., Rummel, U., Strobel, M., Su, Z., Sullivan, R., Tagesson, T., Varlagin, A., Vreugdenhil, M., Walker, J., Wen, J., Wenger, F., Wigneron, J.P., Woods, M., Yang, K., Zeng, Y., Zhang, X., Zreda, M., Dietrich, S., Gruber, A., van Oevelen, P., Wagner, W., Scipal, K., Drusch, M., Sabia, R., 2021. The international soil moisture network: serving earth system science for over a decade. Hydrol. Earth Syst. Sci. 25, 5749–5804.

Dubois, P., Van Zyl, J., Engman, T., 1995. Measuring soil moisture with imaging radars. IEEE Trans. Geosci. Remote Sens. 33, 915–926.

Entekhabi, D., Njoku, E., O'Neill, P., Kellogg, K., Crow, W., Edelstein, W., Entin, J., Goodman, S., Jackson, T., Johnson, J., Kimball, J., Piepmeier, J., Koster, R., Martin, N., McDonald, K., Moghaddam, M., Moran, S., Reichle, R., Shi, J., Spencer, M., Thurman, S., Tsang, L., Van Zyl, J., 2010. The soil moisture active passive (SMAP) mission. IEEE Proc. 98, 704.

Entekhabi, D., Das, N., Njoku, E., Johnson, J., Shi, J., 2016. SMAP L3 Radar/Radiometer Global Daily 9 Km EASE-Grid Soil Moisture. (SPL3SMAP, Version 3). NASA National Snow and Ice Data Center Distributed Active Archive Center, Boulder, Colorado USA.

Fan, D., Zhao, T., Jiang, X., Xue, H., Moukomla, S., Kuntiyawichai, K., Shi, J., 2022. Soil moisture retrieval from Sentinel-1 time-series data over croplands of northeastern Thailand. IEEE Geosci. Remote Sens. Lett. 19, 1–5.

Fang, B., Lakshmi, V., Cosh, M., Liu, P., Bindlish, R., Jackson, T., 2022. A global 1-km downscaled SMAP soil moisture product based on thermal inertia theory. Vadose Zone J. 2, e20182.

Fujii, H., Koike, T., Imaoka, K., 2009. Improvement of the AMSR-E algorithm for soil moisture estimation by introducing a fractional vegetation coverage dataset derived from MODIS data. J. Remote Sens. Soc. Jpn. 29, 282–292.

Fung, A., Chen, K., 2004. An update on the IEM surface backscattering model. IEEE Geosci. Remote Sens. Lett. 1, 75–77.

Fung, A., Li, Z., Chen, K., 1992. Backscattering from a randomly rough dielectric surface. IEEE Trans. Geosci. Remote Sens. 30, 356–369.

Gonzalez-Zamora, A., Sanchez, N., Pablos, M., Martinez-Fernandez, J., 2019. CCI soil moisture assessment with SMOS soil moisture and in situ data under different environmental conditions and spatial scales in Spain. Remote Sens. Environ. 225, 469–482.

Green, J., Seneviratne, S., Berg, A., Findell, K., Hagemann, S., Lawrence, D., Gentine, P., 2019. Large influence of soil moisture on long-term terrestrial carbon uptake. Nature 565, 476–479.

Gruber, A., Scanlon, T., van der Schalie, R., Wagner, W., Dorigo, W., 2019. Evolution of the ESA CCI soil moisture climate data records and their underlying merging methodology. Earth Syst. Sci. Data 11, 717–739.

Hallikainen, M., Ulaby, F., Dobson, M., Elrayes, M., Wu, L., 2007. Microwave dielectric behavior of wet soil-part 1: empirical models and experimental observations. IEEE Trans. Geosci. Remote Sens. 23, 25–34.

Hengl, T., 2018. Clay content in % (kg/kg) at 6 standard depths (0, 10, 30, 60, 100 and 200 cm) at 250 m resolution. In: Zenodo.

Hu, L., Zhao, T., Ju, W., Peng, Z., Shi, J., Rodriguez-Fernandez, J., Wigneron, J., Cosh, M. H., Yang, K., Lu, H., Yao, P., 2023. A twenty-year dataset of soil moisture and

vegetation optical depth from AMSR-E/2 measurements using the multi-channel collaborative algorithm. Remote Sens. Environ. 292.
Hulsman, P., Keune, J., Koppa, A., Schellekens, J., Miralles, D., 2023. Incorporating plant access to groundwater in existing global, satellite-based evaporation estimates. Water Resour. Res. 59, e2022W–e33731W.
Jackson, T., Bindlish, R., Zhao, T., 2011. Justification memo for vegetation index climatology. In: SMAP Science Documents. JPL. February.
Jackson, T., Chan, S., Bindlish, R., Njoku, E., 2018. AMSR-E/AMSR2 Unified L2B Half-Orbit 25 Km EASE-Grid Surface Soil Moisture, Version 1: Boulder.
Jiang, H., Shen, H., Li, X., Li, L., 2022. The 43-Year (1978–2020) Global 9 Km Remotely Sensed Soil Moisture Product. PANGAEA.
Kang, C., Zhao, T., Shi, J., Cosh, M., Chen, Y., Starks, P., Collins, C., Wu, S., Sun, R., Zheng, J., 2020. Global soil moisture retrievals from the chinese FY-3D microwave radiation imager. IEEE Trans. Geosci. Remote Sens. 59, 4018–4032.
Kim, Y., van Zyl, J., 2009. A time-series approach to estimate soil moisture using polarimetric radar data. IEEE Trans. Geosci. Remote Sens. 47, 2519–2527.
Kim, S., Tsang, L., Johnson, J., Huang, S., van Zyl, J., Njoku, E., 2012. Soil moisture retrieval using time-series radar observations over bare surfaces. IEEE Trans. Geosci. Remote Sens. 50, 1853–1863.
Kim, S., Van-Zyl, J., Dunbar, R., Njoku, E., Johnson, J., Moghaddam, M., Tsang, L., 2016. SMAP L3 Radar Global Daily 3 Km EASE-Grid Soil Moisture. (SPL3SMA, Version 3). NASA National Snow and Ice Data Center Distributed Active Archive Center, Boulder, Colorado USA.
Kim, H., Cosh, M., Bindlish, R., Lakshmi, V., 2020. Field evaluation of portable soil water content sensors in a sandy loam. Vadose Zone J. 19.
Konings, A., McColl, K., Piles, M., Entekhabi, D., 2015. How many parameters can be maximally estimated from a set of measurements? IEEE Geosci. Remote Sens. Lett. 12, 1081–1085.
Konings, A., Piles, M., Das, N., Entekhabi, D., 2017. L-band vegetation optical depth and effective scattering albedo estimation from SMAP. Remote Sens. Environ. 198, 460–470.
Koster, R.D., Reichle, R.H., De Lannoy, G.J., Liu, Q., Colliander, A., Conaty, A., Jackson, T., Kimball, J., 2015. Technical Report Series on Global Modeling and Data Assimilation.
Larson, K., Small, E., Gutmann, E., Bilich, A., Braun, J., Zavorotny, V., 2008. Use of GPS receivers as a soil moisture network for water cycle studies. Geophys. Res. Lett. 35.
Lebel, T., Cappelaere, B., Galle, S., Hanan, N., Kergoat, L., Levis, S., Vieux, B., Descroix, L., Gosset, M., Mougin, E., Peugeot, C., Seguis, L., 2009. AMMA-CATCH studies in the Sahelian region of West-Africa: an overview. J. Hydrol. 375, 3–13.
Li, X., Wigneron, J., Fan, L., Frappart, F., Yueh, S.H., Colliander, A., Ebtehaj, A., Gao, L., Fernandez-Moran, R., Liu, X., Wang, M., Ma, H., Moisy, C., Ciais, P., 2022. A new SMAP soil moisture and vegetation optical depth product (SMAP-IB): algorithm, assessment and inter-comparison. Remote Sens. Environ. 271, 112921.
Liu, J., Zhan, X., Hain, C., Yin, J., Fang, L., Li, Z., Zhao, L., 2016. NOAA soil moisture operational product system (SMOPS) and its validations. In: 2016 IEEE International Geoscience and Remote Sensing Symposium (IGARSS), pp. 3477–3480.
Loew, A., Peng, J., Borsche, M., 2016. High-resolution land surface fluxes from satellite and reanalysis data (HOLAPS v1. 0): evaluation and uncertainty assessment. Geosci. Model Dev. 9, 2499–2532.
Loor, G.D., 1968. Dielectric properties of heterogeneous mixtures containing water. J. Microwave Power 3, 67–73.
Ma, C., Li, X., Chen, K., 2019. The discrepancy between backscattering model simulations and radar observations caused by scaling issues: an uncertainty analysis. IEEE Trans. Geosci. Remote Sens. 57, 5356–5372.
Ma, C., Li, X., McCabe, M.F., 2020. Retrieval of high-resolution soil moisture through combination of Sentinel-1 and Sentinel-2 data. Remote Sens. 14, 2303.
Martens, B., Miralles, D., Lievens, H., Van Der Schalie, R., De Jeu, R., Fernández-Prieto, D., Beck, H., Dorigo, W., Verhoest, N., 2017. GLEAM v3: satellite-based land evaporation and root-zone soil moisture. Geosci. Model Dev. 10, 1903–1925.
Mironov, V., Dobson, M., Kaupp, V., Komarov, S., Kleshchenko, V., 2004. Generalized refractive mixing dielectric model for moist soils. IEEE Trans. Geosci. Remote Sens. 42, 773–785.
Mironov, V., Kosolapova, L., Fomin, S., 2009. Physically and mineralogically based spectroscopic dielectric model for moist soils. IEEE Trans. Geosci. Remote Sens. 47, 2059–2070.
Moghaddam, M., Entekhabi, D., Goykhman, Y., Li, K., Liu, M., Mahajan, A., Nayyar, A., Shuman, D., Teneketzis, D., 2010. A wireless soil moisture smart sensor web using physics-based optimal control: concept and initial demonstrations. IEEE J. Select. Top. Appl. Earth Observ. Remote Sens. 3, 522–535.
Muñoz Sabater, J., 2019. ERA5-land hourly data from 1950 to present. In: Copernicus Climate Change Service (C3S). Climate Data Store.
Musial, J., Dabrowska-Zielinska, K., Kiryla, W., Oleszczuk, R., Gnatowski, T., Jaszczynski, J., 2016. Derivation and validation of the high resolution satellite soil moisture products: a case study of the Biebrza Sentinel-1 validation sites, 8, pp. 37–53.
Nguyen, H., Kim, H., Choi, M., 2017. Evaluation of the soil water content using cosmic-ray neutron probe in a heterogeneous monsoon climate-dominated region. Adv. Water Resour. 108, 125–138.
Njoku, E., Jackson, T., Lakshmi, V., Chan, T., Nghiem, S., 2003. Soil moisture retrieval from AMSR-E. IEEE Trans. Geosci. Remote Sens. 41, 215–229.
Oh, Y., Sarabandi, K., Ulaby, F., 1992. An empirical model and an inversion technique for radar scattering from bare soil surfaces. IEEE Trans. Geosci. Remote Sens. 30, 370–381.
Ojo, E.R., Bullock, P.R., L'Heureux, J., Powers, J., McNairn, H., Pacheco, A., 2015. Calibration and evaluation of a frequency domain reflectometry sensor for real-time soil moisture monitoring. Vadose Zone J. 14, 1–12.
O'Neill, P., Bindlish, R., Chan, S., Chaubell, J., Colliander, A., Njoku, E., Jackson, T., 2021. Algorithm Theoretical Basis Document Level 2 & 3 Soil Moisture (Passive) Data Products. NASA.
Osenga, E., Vano, J., Arnott, J., 2021. A community-supported weather and soil moisture monitoring database of the roaring fork catchment of the Colorado River headwaters. Hydrol. Process. 35, e14081.
Owe, M., de Jeu, R., Holmes, T., 2008. Multisensor historical climatology of satellite-derived global land surface moisture. J. Geophys. Res. Earth 113.
Palmisano, D., Mattia, F., Balenzano, A., Satalino, G., Pierdicca, N., Guarnieri, A., 2020. Sentinel-1 sensitivity to soil moisture at high incidence angle and the impact on retrieval over seasonal crops. IEEE Trans. Geosci. Remote Sens. 59, 7308–7321.
Pathe, C., Wagner, W., Sabel, D., Doubkova, M., Basara, J.B., 2009. Using ENVISAT ASAR global mode data for surface soil moisture retrieval over Oklahoma, USA. IEEE Trans. Geosci. Remote Sens. 47, 468–480.
Peng, J., Loew, A., Merlin, O., Verhoest, N., 2017. A review of spatial downscaling of satellite remotely sensed soil moisture. Rev. Geophys. 55, 341–366.
Peng, J., Albergel, C., Balenzano, A., Brocca, L., Cartus, O., Cosh, M., Crow, W., Dabrowska-Zielinska, K., Dadson, S., Davidson, M., de Rosnay, P., Dorigo, W., Gruber, A., Hagemann, S., Hirschi, M., Kerr, Y., Lovergine, F., Mahecha, M., Marzahn, P., Mattia, F., Musial, J., Preuschmann, S., Reichle, R., Satalino, G., Silgram, M., van Bodegom, P., Verhoest, N., Wagner, W., Walker, J., Wegmüller, U., Loew, A., 2021a. A roadmap for high-resolution satellite soil moisture applications-confronting product characteristics with user requirements. Remote Sens. Environ. 252, 112162.
Peng, J., Tanguy, M., Robinson, E., Pinnington, E., Evans, J., Ellis, R., Cooper, E., Hannaford, J., Blyth, E., Dadson, S., 2021b. Estimation and evaluation of high-resolution soil moisture from merged model and earth observation data in the Great Britain. Remote Sens. Environ. 264, 112610.
Peng, Z., Zhao, T., Shi, J., Hu, L., Rodríguez-Fernández, N., Wigneron, J., Jackson, T., Walker, J., Cosh, M., Yang, K., Lu, H., Bai, Y., Yao, P., Zheng, J., Wei, Z., 2024. First mapping of polarization-dependent vegetation optical depth and soil moisture from SMAP L-band radiometry. Remote Sens. Environ. 302, 113970.
Portabella, M., 2022a. SMOS L3 Surface Soil Moisture binned maps at 25 km EASE-2 (V.4.0). CSIC - Instituto de Ciencias del Mar (ICM).
Portabella, M., 2022b. SMOS L4 Surface Soil Moisture downscaled maps at 1 km EASE-2 (reprocessed mode) (V.6.0). CSIC - Instituto de Ciencias del Mar (ICM).
Qiu, J., Crow, W.T., Wagner, W., Zhao, T., 2019. Effect of vegetation index choice on soil moisture retrievals via the synergistic use of synthetic aperture radar and optical remote sensing. Int. J. Appl. Earth Obs. Geoinf. 80, 47–57.
Samaniego, L., Kumar, R., Zink, M., 2013. Implications of parameter uncertainty on soil moisture drought analysis in Germany. J. Hydrometeorol. 14, 47–68.
Samaniego, L., Thober, S., Wanders, N., Pan, M., Rakovec, O., Sheffield, J., Wood, E., Prudhomme, C., Rees, G., Houghton-Carr, H., Fry, M., Smith, K., Watts, G., Hisdal, H., Estrela, T., Buontempo, C., Marx, A., Kumar, R., Aardobservatie, L., Landscape Functioning, G., 2019. Hydrological forecasts and projections for improved decision-making in the water sector in Europe. Bull. Am. Meteorol. Soc. 100, 2451–2472.
Schaefer, G., Cosh, M., Jackson, T., 2007. The USDA natural resources conservation service soil climate analysis network (SCAN). J. Atmos. Ocean. Technol. 24, 2073–2077.
Seneviratne, S., Corti, T., Davin, E., Hirschi, M., Jaeger, E., Lehner, I., Orlowsky, B., Teuling, A., 2010. Investigating soil moisture–climate interactions in a changing climate: a review. Earth Sci. Rev. 99, 125–161.
Serreze, M., Clark, M., Frei, A., 2001. Characteristics of large snowfall events in the montane western United States as examined using snowpack telemetry (SNOTEL) data. Water Resour. Res. 37, 675–688.
Shi, J., Wang, J., Hsu, A.Y., O'Neill, P., Engman, E., 1997. Estimation of bare surface soil moisture and surface roughness parameter using L-band SAR image data. IEEE Trans. Geosci. Remote Sens. 35, 1254–1266.
Shi, J., Jiang, L., Zhang, L., Chen, K., Wigneron, J., Chanzy, A., Jackson, T.J., 2006. Physically based estimation of bare-surface soil moisture with the passive radiometers. IEEE Trans. Geosci. Remote Sens. 44, 3145–3153.
Smith, A., Walker, J., Western, A., Young, R., Ellett, K., Pipunic, R., Grayson, R., Siriwardena, L., Chiew, F., Richter, H., 2012. The Murrumbidgee soil moisture monitoring network data set. Water Resour. Res. 48, 156.
Song, P., Zhang, Y., Guo, J., Shi, J., Zhao, T., Tong, B., 2022. A 1 km daily surface soil moisture dataset of enhanced coverage under all-weather conditions over China in 2003-2019. Earth Syst. Sci. Data 14, 2613–2637.
Su, Z., Wen, J., Dente, L., van der Velde, R., Wang, L., Ma, Y., Yang, K., Hu, Z., 2011. The Tibetan plateau observatory of plateau scale soil moisture and soil temperature (Tibet-Obs) for quantifying uncertainties in coarse resolution satellite and model products. Hydrol. Earth Syst. Sci. 15, 2303–2316.
Thober, S., Kumar, R., Sheffield, J., Mai, J., Schäfer, D., Samaniego, L., 2015. Seasonal soil moisture drought prediction over Europe using the north American multi-model ensemble (NMME). J. Hydrometeorol. 16, 2329–2344.
Topp, G., Davis, J., Annan, A., 1980. Electromagnetic determination of soil water content: measurements in coaxial transmission lines. Water Resour. Res. 16, 574–582.
Torres, R., Snoeij, P., Geudtner, D., Bibby, D., Davidson, M., Attema, E., Potin, P., Rommen, B., Floury, N., Brown, M., Traver, I.N., Deghaye, P., Duesmann, B., Rosich, B., Miranda, N., Bruno, C., L'Abbate, M., Croci, R., Pietropaolo, A., Huchler, M., Rostan, F., 2012. GMES Sentinel-1 mission. Remote Sens. Environ. 120, 9–24.
Ulaby, F., Long, D., Blackwell, W., Elachi, C., Fung, A., Ruf, C., Sarabandi, K., Zebker, H., Van-Zyl, J., 2015. Microwave Radar and Radiometric Remote Sensing. The University of Michigan Press.

Ullmann, T., Jagdhuber, T., Hoffmeister, D., May, S., Baumhauer, R., Bubenzer, O., 2023. Exploring Sentinel-1 backscatter time series over the Atacama Desert (Chile) for seasonal dynamics of surface soil moisture. Remote Sens. Environ. 285, 113413.
Van der Velde, R., Benninga, H., Retsios, B., Vermunt, P., Salama, M., 2023. Twelve years of profile soil moisture and temperature measurements in Twente, the Netherlands. Earth Syst. Sci. Data 15 (4), 1889–1910.
Veci, L., Prats-Iraola, P., Scheiber, R., Collard, F., Fomferra, N., Engdahl, M., 2014. The Sentinel-1 toolbox. In: In: Proceedings of the IEEE International Geoscience and Remote Sensing Symposium (IGARSS), 2012-07-14 - 2012-07-18. Canada, Québec.
Vereecken, H., Huisman, J., Bogena, H., Vanderborght, J., Vrugt, J., Hopmans, J., 2008. On the value of soil moisture measurements in vadose zone hydrology: a review. Water Resour. Res. 44, 1–21.
Vergopolan, N., Chaney, N., Beck, H., Pan, M., Sheffield, J., Chan, S., Wood, E., 2020. Combining hyper-resolution land surface modeling with SMAP brightness temperatures to obtain 30-m soil moisture estimates. Remote Sens. Environ. 242, 111740–111755.
Vergopolan, N., Chaney, N., Pan, M., Sheffield, J., Beck, H., Ferguson, C., Torres-Rojas, L., Sadri, S., Wood, E., 2021. SMAP-HydroBlocks, a 30-m satellite-based soil moisture dataset for the conterminous US. Sci. Data 8, 264.
Wagner, W., 1998. Soil moisture retrieval from ERS scatterometer data, Vol. 49. Inst. für Photogrammetrie u. Fernerkundung d. Techn. Univ.
Wagner, W., Lemoine, G., Rott, H., 1999. A method for estimating soil moisture from ERS scatterometer and soil data. Remote Sens. Environ. 70, 191–207.
Wagner, W., Hahn, S., Kidd, R., Melzer, T., Bartalis, Z., Hasenauer, S., Figa-Saldaña, J., de Rosnay, P., Jann, A., Schneider, S., Komma, J., Kubu, G., Brugger, K., Aubrecht, C., Züger, J., Gangkofner, U., Kienberger, S., Brocca, L., Wang, Y., Blöschl, G., Eitzinger, J., Steinnocher, K., 2013. The ASCAT soil moisture product: a review of its specifications, validation results, and emerging applications. Meteorol. Z. 22, 5–33.
Wagner, W., Lindorfer, R., Melzer, T., Hahn, S., Bauer-Marschallinger, B., Morrison, K., Calvet, J., Hobbs, S., Quast, R., Greimeister-Pfeil, I., 2022. Widespread occurrence of anomalous C-band backscatter signals in arid environments caused by subsurface scattering. Remote Sens. Environ. 276, 113025.
Wang, J.R., Schmugge, T., 1980. An empirical model for the complex dielectric permittivity of soils as a function of water content. IEEE Trans. Geosci. Remote Sens. 18, 288–295.
Wang, Z., Zhao, T., Shi, J., Wang, H., Ji, D., Yao, P., Zheng, J., Zhao, X., Xu, X., 2023. 1-km soil moisture retrieval using multi-temporal dual-channel SAR data from Sentinel-1 a/B satellites in a semi-arid watershed. Remote Sens. Environ. 284, 113334.
Wigneron, J., Li, X., Frappart, F., Fan, L., Al-Yaari, A., De Lannoy, G., Liu, X., Wang, M., Le Masson, E., Moisy, C., 2021. SMOS-IC data record of soil moisture and L-VOD: historical development, applications and perspectives. Remote Sens. Environ. 254, 112238–112258.
Yao, P., Lu, H., Shi, J., Zhao, T., Yang, K., Cosh, M., Gianotti, D., Entekhabi, D., 2021. A long term global daily soil moisture dataset derived from AMSR-E and AMSR2 (2002-2019). Sci. Data 8.
Yao, P., Lu, H., Zhao, T., Wu, S., Peng, Z., Cosh, M., Jia, L., Yang, K., Zhang, P., Shi, J., 2023. A global daily soil moisture dataset derived from Chinese FengYun microwave radiation imager (MWRI) (2010-2019). Sci. Data 10, 133.
Zacharias, S., Bogena, H., Samaniego, L., Mauder, M., Fuss, R., Puetz, T., Frenzel, M., Schwank, M., Baessler, C., Butterbach-Bahl, K., Bens, O., Borg, E., Brauer, A., Dietrich, P., Hajnsek, I., Helle, G., Kiese, R., Kunstmann, H., Klotz, S., Munch, J., Papen, H., Priesack, E., Schmid, H., Steinbrecher, R., Rosenbaum, U., Teutsch, G., Vereecken, H., 2011. A network of terrestrial environmental observatories in Germany. Vadose Zone J. 10, 955–973.
Zhang, Y., Liang, S., Ma, H., He, T., Wang, Q., Li, B., Xu, J., Zhang, G., Liu, X., Xiong, C., 2023. Generation of global 1 km daily soil moisture product from 2000 to 2020 using ensemble learning. Earth Syst. Sci. Data 15, 2055–2079.
Zhao, T., Shi, J., Lv, L., Xu, H., Chen, D., Cui, Q., Jackson, T., Yan, G., Jia, L., Chen, L., Zhao, K., Zheng, X., Zhao, L., Zheng, C., Ji, D., Xiong, C., Wang, T., Li, R., Pan, J., Wen, J., Yu, C., Zheng, Y., Jiang, L., Chai, L., Lu, H., Yao, P., Ma, J., Lv, H., Wu, J., Zhao, W., Yang, N., Guo, P., Li, Y., Hu, L., Geng, D., Zhang, Z., 2020. Soil moisture experiment in the Luan River supporting new satellite mission opportunities. Remote Sens. Environ. 240, 111680.
Zheng, J., Zhao, T., Lü, H., Shi, J., Cosh, M., Ji, D., Jiang, L., Cui, Q., Lu, H., Yang, K., Wigneron, J., Li, X., Zhu, Y., Hu, L., Peng, Z., Zeng, Y., Wang, X., Kang, C., 2022. Assessment of 24 soil moisture datasets using a new in situ network in the Shandian river basin of China. Remote Sens. Environ. 271, 112891.
Zheng, C., Jia, L., Zhao, T., 2023. A 21-year dataset (2000−2020) of gap-free global daily surface soil moisture at 1-km grid resolution. Sci. Data 10, 139.
Zhu, L., Walker, J.P., Ye, N., Rüdiger, C., 2019. Roughness and vegetation change detection: a pre-processing for soil moisture retrieval from multi-temporal SAR imagery. Remote Sens. Environ. 225, 93–106.
Zhu, L., Walker, J., Shen, X., 2020. Stochastic ensemble methods for multi-SAR-mission soil moisture retrieval. Remote Sens. Environ. 251, 112099.